AN ABSTRACT OF THE THESIS OF

Sonia Ahrens for the degree of Master of Science in Bioengineering presented on March 12, 2021.

Title: Precision Medicine for the Intervertebral Disc: Image Processing and Computational Modeling of Disc Degeneration to Inform Patient-Specific Therapies

Abstract approved: _____

Morgan B. Giers

The human intervertebral disc is a deceptively simple structure which plays an essential role in human movement. Even slight changes to the disc microenvironment can have far reaching consequences, particularly when these changes result in disc degeneration and herniation. Degeneration is increasingly tied to lower back pain; better understanding this complex relationship could enable more informed treatments and better outcomes for patients suffering from low back pain. The overall aim of the work presented here is to investigate tools and techniques which might aid in patient evaluation, for use in both research and clinical settings. Specifically, this includes (1) development of a patient-specific finite element model of nutrient transport in the disc, and (2) quantitative comparison of a novel imaging modality (apparent diffusion coefficient mapping) to established modalities for disc visualization. In the first investigation, results of the patient-specific model showed distinct diffusion behavior between patients, even within discs of the same degeneration grade, indicating the importance of the patient-specific diffusivities to the accurate prediction of nutrient availability in the disc. In the second investigation, the results indicated a general sensitivity of both modalities to degeneration of the NP. However, significant differences were found between the modalities at measuring the same features, indicating that the two modalities have fundamentally different capabilities for IVD visualization and implying that one is more accurate than the other. Validating this will be the focus of future work.

Precision Medicine for the Intervertebral Disc:
Image Processing and Computational Modeling of Disc
Degeneration to Inform Patient-Specific Therapies

by
Sonia Ahrens

A THESIS

submitted to

Oregon State University

in partial fulfillment of
the requirements for the
degree of

Master of Science

Presented March 12, 2021
Commencement June 2021

Master of Science thesis of Sonia Ahrens presented on March 12, 2021.

APPROVED:

_____

Major Professor, representing Bioengineering

_____

Head of the Department of Chemical, Biological & Environmental Engineering

_____

Dean of the Graduate School

I understand that my thesis will become part of the permanent collection of Oregon State University libraries. My signature below authorizes release of my thesis to any reader upon request.

_____

Sonia Ahrens, Author

ACKNOWLEDGEMENTS

TABLE OF CONTENTS

LIST OF FIGURES

LIST OF TABLES

LIST OF APPENDIX FIGURES

LIST OF APPENDIX TABLES

Chapter 1: Introduction & Literature Review

Aims and Thesis Overview

An overview of the topics covered in the present work is shown in **Figure 1.1.** The general purpose of the work presented here is to evaluate methods used to clinically image and model the human intervertebral disc (IVD). Chapter 1 provides an overview of key topics and literature relevant to the work presented here. Chapter 2 showcases a novel method for evaluating spinal pathology using patient-specific finite element modeling of IVD transport. Chapter 3 quantitatively compares two magnetic resonance imaging (MRI) modalities – ADC mapping and T2$_w$ imaging – for visualizing the IVD. Chapter 4 presents general conclusions, including a summary of the work, its relevance to the field and to future research. An index of abbreviations used in this work is provided in **Table A1.1** of **Appendix 1.**
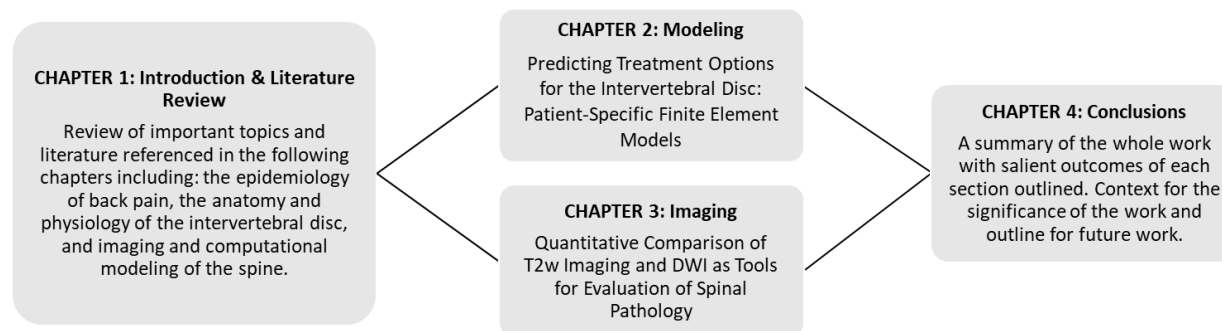
Figure 1.1 – Thesis topics overview. This thesis is compiled in manuscript format.

Back Pain: Epidemiology, Treatment and The Myth of "One Size Fits All"

Back pain is the leading cause of disability worldwide.[1] Experts estimate that up to 80% of the population will experience some form of back pain[2] and a recent review determined the yearly incidence of low back pain to be as high as 36%.[3] It was also noted that most people who experience activity-limiting low back pain go on to have recurrent episodes, with estimates of annual recurrence ranging from 24% to 80%. Despite its pervasiveness, the cause of lower back pain (LBP) frequently goes unidentified, with up to 90% of cases worldwide qualifying as Non-Specific Low Back Pain (NSLBP) or pain that currently has no clinically

discernable cause.[4] Intervertebral disc degeneration has been implicated as one possible cause of this pain,[5–8] though a consistent correlation between early stage degeneration (as observed on medical imaging) and incidence of pain has yet to be established.[9] Disc degeneration has also been implicated as the driving force behind the observed age-dependence in many cases of low back pain,[10] the later stages of which frequently involve disc bulging and herniation.

Treatments for lower back pain generally fall into one of two categories: conservative or invasive. Different treatments are recommended depending on whether the low back pain is acute (<4 weeks), subacute (4 to 12 weeks). or chronic (>12 weeks), and whether the source is known (specific) or unknown (non-specific).[11] Conservative therapies are somewhat general, and include medication (analgesics, NSAIDS, muscle relaxants etc.), steroid injection, radiofrequency denervation, massage and acupuncture, behavioral therapy, chiropractic treatment, physical/exercise therapy, traction therapy and use of various passive rehabilitation modalities (e.g. transcutaneous electrical nerve stimulation (TENS), ultrasound and iontophoresis). A more comprehensive review of these treatments and their reported outcomes is provided in **Table 1.1.** Invasive therapies are more targeted; surgeries are selected specifically for certain conditions or indications. These surgeries include vertebroplasty and kyphoplasty for fractured vertebra, spinal decompression/laminectomy for spinal stenosis, foraminotomy for pinched nerve roots, and discectomy/microdiscectomy, nucleoplasty, artificial disc replacement and spinal fusion for herniated discs.[12] Notably, there are several surgical options available for herniated discs, which can make choosing an appropriate treatment difficult. These options and their reported outcomes are outlined in **Table 1.2**. For **Tables 1.1** and **1.2**, the table scores were derived primarily from Qassem et al. (2017),[11] Malfliet et al. (2019)[13] and other relevant sources.[14–35] The outcome measures are based on metrics described in Delitto et al. (2012),[36] the International Consortium on Health Outcomes Measurements (ICHOM) reference guide (version 2.0.3),[37] Resnik and Dobrzykowski (2003),[38] and Stamm et al. (2019).[39] The various outcome metrics were grouped into four categories: 1) pain, 2) function, 3) patient satisfaction and quality of life and 4) adverse events. Included in the "pain" category are the metrics of the Visual Analogue Scale (VAS)

and the Global Assessment (GA). The "function" category encompasses the following metrics: Activity Limitation (AL), the Oswestry Disability Index (ODI), Work Status, the Work Limitations Questionnaire (WLQ), the Work Ability Index (WAI), and the Roland-Morris Disability Questionnaire (RMQ/RMD). The "patient satisfaction and quality of life" category includes the following: the McNab Criteria, the Canadian Occupational Performance Measure (COPM), the Zung Depression Scale, the Wilson-Cleary Health Related Quality of Life (HRQL), the short form (SF-36 & SF-12) and EQVOL-5 questionnaires. Scores in the table correspond to the degree of influence of the treatment on the patient outcome metric, and the colors indicate the nature of the effect and its magnitude, where green is strongly positive and red is strongly negative. Specifics of the number and color grading system are shown in **Table 1.3.** The scores in the adverse event category reflect a qualitative combination of the severity and frequency of the adverse event occurrence. Severity of the adverse event was categorized based on the Common Terminology Criteria for Adverse Events (CTCAE)[40] outlined by the NIH, in addition to the Spine Adverse Events Severity System (SAVES) outlined by Rampersaud et al. (2010).[41] The resulting categorization system is shown in the **Table A3.1** in **Appendix 3**.

Unfortunately, even when following the best practice guidelines (BPG) for treating low back pain, the resulting patient outcomes often leave much to be desired. As demonstrated in **Tables 1.1** and **1.2**, many of these treatments have insufficient evidence of efficacy or show limited or variable success.[42] This is especially true in the case of non-specific lower back pain, where evidence-based practice is often hindered by the lack of a more specific diagnosis. There are also various confounding factors which make it difficult to directly assess treatment efficacy. These factors include inappropriate use or execution of the treatment,[42,43] the placebo effect,[44,45] and the large role psychosocial factors play in pain perception.[46,47] For example, many surgical interventions also show limited efficacy even for "specific" LBP; this may have less to do with the efficacy of the surgery itself and more to do with inappropriate use of the surgery or poor execution of the surgical technique. This is demonstrated by the fact that, despite

Table 1.1 – Outcomes for conservative treatments of acute and chronic LBP. Outcome categories may be fulfilled by various metrics, overall scores range from 0 to 1. A score of 0 indicates no difference from the control group (often placebo). Interventions with unknown or insufficient evidence were left empty.

Intervention	Acute LBP (Short Term)				Chronic LBP (Long Term)			
	Pain	Function	Patient Satisfaction/ Quality of Life	Adverse effects	Pain	Function	Patient Satisfaction/ Quality of Life	Adverse effects
Pharmacologic								
NSAIDs	0.25	0.25		0.25	0.25	0		0.25
Acetaminophen	0	0		0				0
Opioid analgesics				0.5	0.25	0.25		0.75
Antidepressants				0.25	0	0		0.5
Skeletal Muscle Relaxants (SMRs)	0.25			0.5	0.25			0.5
Benzodiazepines				0.5				0.75
Corticosteroids	0	0			0	0		
Antiepileptic drugs								
Non-Pharmacologic: Passive/Stimulation Therapies								
Superficial Heat/Cold	0.5	0.5		0				0
Steroid injection	0	0						
Acupuncture	0.25	0		0	0.5	0.25		0
Percutaneous Electrical Nerve Stimulation								
Transcutaneous electrical nerve stimulation (TENS)	0	0		0.25	0.25	0.25		0.25
Radiofrequency Denervation	0	0						
Ultrasound	0	0		0	0	0		0
Iontophoresis	0	0						
Interferential Therapy								
Low-level laser therapy (LLLT)	1	0.5			0.25	0.25		
Short-wave diathermy								
Lumbar supports/braces	0.5	0.5		0	0	0		0
Traction Therapy				0				0
Non-Pharmacologic: Physical/Active Therapies								
Massage	0.5	0.5		0	0	0		0
Spinal Manipulation/Chiropactic	0	0.25		0.25	0	0.25		0.25
Physical therapy	0.25	0.25			0.5	0.25		
General Exercise	0	0		0	0.25	0.25		0
Exercise: Flexibility/Range of Motion	0	0.25		0.25	0.75	0.625		0.25
Exercise: Aerobic	0	0		0	1	0.75		0
Exercise: Strengthening/Stabilization	0.25	0		0	1	1	0.75	0
Behavioral								
Bed Rest	0	0		0.5	0	0		0.5
Psychological therapies	0.25	0.25		0	0.5	0.5		0

advances in surgical technology, the rates of failed back surgery have not declined.[48] Furthermore, all these treatments are aimed at addressing the symptoms of degeneration, rather than the root cause. There is a growing area of research dedicated to biological treatments aimed at halting and even reversing disc degeneration itself, but these therapies are in early stages of development and are not currently being used routinely in the clinic.

Table 1.2 – Minimally invasive and invasive interventions for LBP. Outcome categories may be fulfilled by various metrics, overall scores range from 0 to 1. A score of 0 indicates no difference from the control group (often placebo).

Intervention	Pain	Function	Patient Satisfaction/ Quality of Life	Adverse effects
Surgical				
Microdiscectomy	1	0.75	1	0.6
Artificial IVD	1	0.75	0.75	0.7
Discectomy	0.75	0.5	1	0.7
Laminectomy	0.5	0.75	0.75	0.7
Fusion	0.5	0.5	0.75	0.75

As we continue to look for more and better treatments for LBP, this distinction is of great importance, especially in the case of surgical interventions. Performing an inappropriate or unnecessary surgery has the potential to send patients down a pathway of repeated failed back surgeries, referred to as failed back surgery syndrome.[48,49] This could be prevented through pursuing more targeted, patient-specific treatment and abandoning a "one size fits all" approach. Here, "patient-specific" is a twofold idea, encompassing both more robust patient evaluation methods, and more personalized treatments tailored to the patient's specific biomechanics, environmental influences (e.g. occupation) and personal priorities (e.g. children, hobbies etc.). This should enable physicians to better meet patient's expectations for treatment,[50] and avoid wasting time and money on inappropriate treatment strategies and resulting complications.

Table 1.3 – Scoring rubric for Tables 1.1 and 1.2.

Adverse Event	Unknown/ Insufficient Evidence:	No significant adverse effect	Mild adverse event	Moderate adverse event	Severe adverse event	Serious adverse event
		0	0.25	0.5	0.75	1
Patient Satisfaction	Unknown/ Insufficient Evidence:	Very Disatisfied	Mildly Dissatisfied	Neutral	Mildly Satisfied	Very Satisfied
		0	0.25	0.5	0.75	1
Pain & Function	Unknown/ Insufficient Evidence:	None/ Insignificant*	Small effect	Moderate effect	Substantial effect	Large effect
		0	0.25	0.5	0.75	1

Anatomy and Physiology of the IVD

The IVD is the largest avascular structure in the human body.[51] The IVD's primary substructures include the annulus fibrosus (AF), nucleus pulposus (NP) and cartilaginous endplate (CEP). External structures include the vertebral bodies (made up of cancellous bone surrounded by a shell of cortical bone) which interface with the discs through the bony endplate (BEP). A diagram of the complete structure from Huang et al. (2014)[5] is provided in **Figure A2.1** of **Appendix 2**. Disc homeostasis relies primarily on the mechanism of diffusion through the CEP, both to deliver nutrients (glucose and oxygen, among others) to cells in the NP, and AF and to remove unwanted metabolites (lactic acid, among others) from the disc tissue. The primary function of the discs – which make up 15–20 % of the length of the spinal column – is absorbing biomechanical forces and allowing movement of the spinal column.[52] By design, these structures must endure regular mechanical loading, which includes extremes of both loading (ex. carrying items) and unloading (ex. hanging upside-down). This loading has been shown to have a mixed influence on cell viability in the disc;[53] loading decreases disc height, which reduces the diffusion distance for nutrients traveling from the CEP to cells at the center of the disc, but also decreases the fluid content in the disc, which reduces solute diffusivities and increases cell metabolism, leading to further buildup of metabolic byproducts like lactic acid.[54]

This unique structure places IVD cells under a variety of environmental stresses, including perpetual nutrient deprivation, buildup of metabolic byproducts, extreme pH and mechanical strains. Disc cells – particularly those in the center axial plane – contend with large nutrient diffusion distances and slow diffusion speeds. These issues are compounded by physiological/structural changes due to aging or illness which can impair access to vasculature for the disc to receive nutrients and offload wastes. Impaired blood supply is a symptom of numerous diseases, including atherosclerosis of arteries in the lumbar spine and buildup of atherosclerotic plaques (common symptoms of smoking and diabetes[55,56]), sickle cell anemia, and structural changes including occlusion of the marrow spaces, calcification of the endplate, endplate sclerosis, Modic changes, Schmorl's nodes or endplate lesions.[5] These factors can prevent adequate nutrients from reaching IVD cells, which are already relatively sparse, leading to suppressed cell activity and tissue maintenance, and eventually cell death.[57,58] As the rate of cell death increases beyond the rate of cell generation, the tissue will begin to degenerate, which can lead to issues like disc bulging and herniation.

Mathematical/Computational Modeling of the Spine – Literature Review

Several groups have tackled modeling the metabolism of the intervertebral disc: J.G. Urban,[59,60] Stephen J. Ferguson,[61] Andrea Malandrino,[62] and Alicia R. Jackson,[63] among others[64–66]. These groups have each characterized key properties related to IVD metabolism and transport, some of which will be included in the model developed here. Bibby (2005)[59] established that excised disc tissue (in culture medium exposed to air and at pH 7.4) behaves very differently from that found in vivo, where oxygen, glucose, and pH are all low. Namely, oxygen consumption and glycolysis dropped markedly under these conditions, and equations were derived that satisfactorily predicted this behavior. The group did not account for the effects of mechanical stress/strain on cell consumption and on diffusivities due to a lack of data. Malandrino (2011)[62] addressed this topic, and found mechanical loading significantly influenced oxygen and lactate concentration when large and prolonged volume changes were applied due to changes to both the tissue diffusivity and diffusion distances within the disc. However, excessive or prolonged loading

was found to trigger a drop in cell density and a decrease in NP swelling pressure due to loss of proteoglycans, both of which are detrimental to the disc. With respect to oxygen deprivation, this group noted that the location of "critical regions" (critically low oxygen levels) depended strongly on patient-specific characteristics. This group did not consider local cell matrix synthesis and viability in their investigation, and therefore the behavior of glucose was ignored. A similar omission was also made by Zhu (2012). [64]

However, Ferguson (2004)[61] found that loading-induced convection of fluid in the disc did not actually enhance the transport of low-weight solutes and had minimal influence on the transport of large molecular-weight solutes. Though, it should be noted fluid flow and solute transport were not directly coupled in this model. Our group's previous findings also support this conclusion: the finite element model developed in Munter et. al (2016)[66] indicated no significant difference between a traction-treated disc and a regular degenerated disc. In fact, the *in-vitro* traction study which informed the Munter et. al (2016) model actually showed a significant decrease in nutrient flow through traction-treated discs, relative to untreated discs. One possible explanation can be demonstrated with an analogy to hyperventilation: if the nutrient-rich fluid moves past the tissue too fast there may not be time for adequate nutrient transport. However, the Munter et. al (2016) model behavior seems to indicate that certain biomechanical aspects of physiologic stretching were not captured in the simplified math model, and further characterization is necessary *in vivo* to understand exact structural changes that occur during loading/unloading. Other groups have further characterized the behavior of metabolites in the disc, and their interactions. Soukane (2007)[60] coupled model equations for glucose, oxygen and lactate. This study found that nutrient concentrations could fall below levels required to maintain cellular activity or viability under the following conditions: (1) a loss of endplate permeability, (2) increased rates of oxygen and glucose consumption or lactic acid production, or (3) a fall in diffusivity due to long-term dehydration. This model incorporated work from Jackson (2009)[63] which established fixed charge densities (FCD) for IVD tissues using a two-point conductivity approach. Specifically, Jackson (2009) determined that the FCD of

AF tissue is significantly lower than that of NP tissue, a property which was incorporated into boundary conditions of the Soukane model. However, it should be noted that Jackson's model for ion diffusivity does not account for relative water content of the tissue, nor attempt to develop a relationship between the two properties.

Together, these investigations were paramount in establishing the groundwork of the current investigation. However, they each possess several limitations, some of which the current work attempts to address. Most significantly, the studies were unable to capture the extreme variability in solute distribution which exists between patients, even between discs of the same degeneration grade (as will be demonstrated here). This variability is inherent to the patient depending on their health status (genetics, metabolism, pre-existing conditions, etc.) and behaviors (work, hobbies, activity level, etc.). These factors influence myriad variables in the disc microenvironment, including the thickness of the endplates, the quality/magnitude of blood supply, the specific disc sizing and tissue ratios, and daily loading patterns and intensity.

Imaging & Image Processing of the Spine – Literature Review

Imaging has become a primary means of data collection across clinical research and medicine, primarily due to its non-invasive nature, which enables internal structures to be visualized without need for surgery. For the spine, clinical imaging is now standard practice for the evaluation and diagnosis of patients with a wide range of possible spine-related ailments, ranging from musculoskeletal disorders (MSD) and lower back pain (LBP) to acute trauma.[68] Though, it is important to note that imaging has been shown to have less direct correlation to outcomes in cases of non-specific low back pain,[36,69–71] mainly due to confounding factors including the strong role psychosocial factors play in pain perception.[46,47] However, for patients with "red flag" indications for conditions which would require immediate surgery or in cases where conservative therapy proves ineffective, imaging is often essential. These "red flag" conditions would include instances of spinal cord or nerve root compression (Cauda equina syndrome), spinal fractures, tumors, back-related infections and abdominal aneurysms.[36]

Many imaging modalities are used for evaluating the lumbar spine, including (in order of expense) radiographic imaging (X-rays), ultrasonography, nuclear medicine, computerized tomography (CT) scans and magnetic resonance imaging (MRI).[72] Radiographs are typically the first in line if imaging is deemed necessary and musculoskeletal disorders are suspected. This is because X-ray is widely available, and less expensive than other modalities, though it is not recommended for use with pregnant patients.[68] Radiographs can be used to look for fractures/dislocations and assess features like vertebral body height and disc space, and a decrease in the latter has been shown to be associated with lower back pain.[73] Diagnostic ultrasound is another relatively inexpensive modality which is safe for use in pregnant patients as well as newborns where it can be used to look for congenital abnormalities of the spinal cord. In adults with LBP, its utility is somewhat limited; it can be used to look for inflammation, cysts, damage or degenerative changes in the paralumbar muscles and connective tissues or can be used measure the spinal canal size.[74,75] Nuclear medicine involves using a radioactive tracer to scan bone and evaluate metabolic activity and severity of metastatic diseases, though it can also be used to investigate cases of suspected spondylodiscitis.[68] CT is a powerful (and expensive) modality which can be used to assess bone and implanted materials in great detail and is frequently used in cases of complex trauma/fractures or lumbar stenosis.[74] CT can be used as an alternative for patients who have contraindications for MRI, such as for patients with metallic implants, however, like X-ray, it is not safe for use with pregnant patients due to concerns of radiation impact on fetal development.

Finally, while MRI is the most expensive of the modalities available, it is perhaps the most sensitive to subtle differences/changes in soft tissue. As such, it has become the gold standard for evaluation of the lumbar spine, particularly in cases of suspected lumbar disc herniation.[72] MRI has been shown to be very adept at identifying and locating herniated disc tissue[36,69] which is necessary when assessing the need for surgical intervention and for surgical planning. MRI also offers the added benefit of containing multiple modalities within itself, which is achieved simply by varying the specific settings and sequences of radiofrequencies used. Depending on the pulse intensity and repetition time (RT), different echo

times (ET) will result based on tissue properties.[74] These sequences can be tailored to maximize contrast of certain substructures or to extract specific tissue properties, like tissue hydration and diffusivity. For clinical evaluation of the lumbar spine, T1 weighted ($T1_w$) and T2 weighted ($T2_w$) images are the primary MRI modalities used, and images are typically taken in the sagittal or axial planes.[69] More niche modalities are used in spine research, particularly for quantitative image processing studies, including T1 rho (T1ρ) imaging,[76–78] T2/T2* mapping,[79–82] MR spectroscopy[83] and diffusion-weighted imaging (DWI)[84,85], among others.

By extension, image processing has also become an essential part of both medicine and clinical research. There are two main types of data to glean from image processing: qualitative data and quantitative data. For the spine, qualitative metrics would include assessment of the various grading systems for intervertebral disc degeneration. Upwards of forty different grading systems exist for the intervertebral disc,[86] based on various data types including: macroscopic anatomy (e.g. the Thompson grade[87]), histology (e.g. the Boos classification[88]), radiography (e.g. the Lane grading system[89]), magnetic resonance imaging (e.g. the Pfirrmann grade[90] demonstrated in **Figure 1.2** and **Figure A2.2**) and discography (e.g. the Gunzburg grading system[91]). When it comes to quantitative metrics, these include measurements like disc height index (DHI),[92] sagittal range of motion (SROM),[93] central angle of lumbar lordosis[94] and pixel signal intensity.[95]

These various measures, both qualitative and quantitative, can guide clinical treatment and be used in research. Specifically, they are frequently used to document and characterize the process of disc degeneration, and also to establish correlations between diagnostic indicators and patient outcomes. This area of research is intended to inform clinical practice and enable development of more efficacious treatment plans. However, if made at all, measurements are being done by hand in a clinical setting. Manual methods of measurement are prone to high inter- and intra-rater variability, particularly as the complexity of the measurement increases, which can compromise the utility of performing such measurements altogether. Recent studies involving image processing of the spine have reported intra-

rater reliability, quantified by intra-class correlation coefficients (ICC), ranging from 0.82 to 0.99 and

inter-rater reliabilities ranging from as low as 0.45 to 0.98.[96–99] These studies also highlight how the

imaging modality, the specific type of measurement being made and raters level of experience (novice

vs. expert) can also greatly influence the reliability of the measurement.
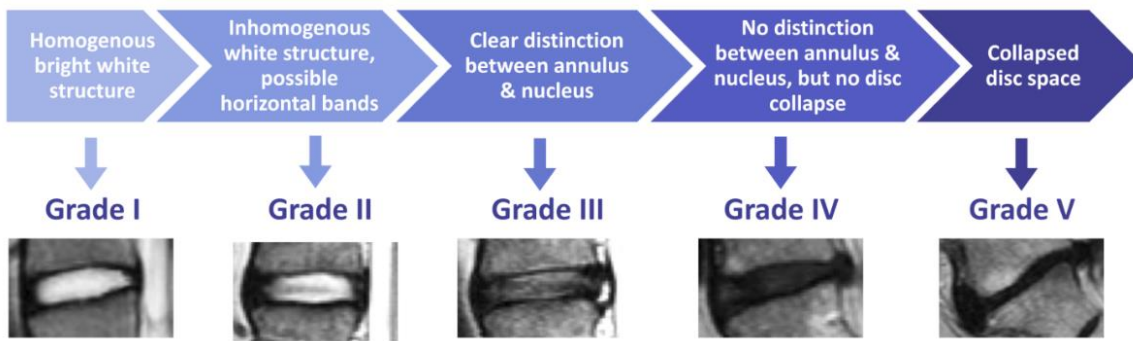
Figure 1.2 – Evaluation of the lumbar spine using MRI and the radiological Pfirrmann grade, adapted from Lootus et al. (2014)[67]

In addition to issues of measurement variability, there is also an issue with consistency of practice/use of

clinical image measurements. These measurements can be very time intensive, which often dissuades

medical professionals from doing them at all due to the impediment to their clinical workflow. For these

reasons, there is increasing effort being made in both research and industry to develop techniques to

streamline image processing. This typically involves user-guided, semi-automatic or fully-automatic

processing protocols which require minimal to no human input.[96] User-guided and semi-automated

protocols involve the use of techniques and tools like pixel intensity-based thresholding,[100] active

contouring/edge detection,[101] clustering algorithms,[102] region-based methods,[103] watershed

transformations,[104] region growing algorithms,[105] B-spline active surface segmentation[106] and deformable

models.[107–109] Fully automated processing is achieved using machine learning (ML) algorithms which,

once developed and validated, can functionally eliminate the need for user input.[110] The merit of these

techniques is twofold: image processing speed is increased while the inter- and intra-rater variability is

decreased.

Chapter 2: Modeling

Introduction

Current treatments for disc degeneration are primarily aimed at addressing the symptoms of degeneration and herniation, and not degeneration itself, thereby limiting the success of these strategies.[49] Novel alternative treatments focus on targeting the molecular pathways of extracellular matrix (ECM) degeneration. Degeneration is a natural process which is strongly associated with aging, and recent research indicates it is intricately linked with cell senescence.[111] Senescent cells undergo cell-cycle arrest, usually coupled with distinctive phenotypic changes related to their metabolism, chromatin organization, secretome production and tumor-suppression activity.[112] These are implicated in degeneration of the ECM, both due to decreased cell density (i.e. less cells performing matrix maintenance and renewal) and secretion of inflammatory molecules which have been tied to degeneration of the matrix which gives the IVD its distinctive biomechanical properties. Current methods of counteracting cell senescence primarily involve removing or replacing senescent cells with healthy and proliferative cells,[113,114] increasing/upregulating anabolic pathways (e.g. by introducing growth factors),[115–117] or decreasing and downregulating catabolic or apoptotic pathways.[118–120] However, the interplay between increasing the cell activity/ density in the disc and subsequent changes to nutrient availability is frequently overlooked during implementation of these strategies. This is a critical consideration; IVD-specific nutrient availability must be accounted for to prevent accidentally increasing nutrient demands beyond the capacity of system and causing a cell population collapse.

In the current work, IVD transport models were developed with the goal of predicting the patient-specific nutrient distribution in the disc via integration of real patient data into key model parameters; namely, diffusion behavior within the disc nucleus. Historically, the nucleus shows high variability between discs, even at similar stages of degradation, and therefore should sufficiently showcase any unique patient-specific trends.[121,122] Patient data was collected with MRI, and included diffusion coefficients and general morphology of the disc structure. Incorporating patient data enables many unique disc characteristics to

be accounted for simultaneously, which would otherwise need to be characterized independently and then separately applied. The rest of the model was built based on previously developed models for IVD, which were outlined previously. Pending further development, this model has great potential, for both lab and clinic applications. Patient-specific models could be used in a clinical setting to inform patient treatments – i.e., determine if a given disc is a good candidate for biological therapies, and to tailor the treatments to the specific nutrient environment and limitations of the disc. These models could also be used in clinical research, to investigate the utility or appropriate dosing for new biological therapies.

Materials & Methods

Patient Data Collection

The full MRI methodology used here can be found in Belykh 2017.[123] Briefly: T1-weighted, T2-weighted and DWI images were taken of 100 consecutive patients admitted to the spinal surgery service at the Irkutsk Scientific Center of Surgery and Traumatology for vertebral fusion surgeries. This population excluded patients with spinal pathologies at levels other than lumbar, or those with tumors or vascular pathology. Imaging was performed on a 1.5 T Siemens Magnetom Essenza scanner (Siemens Healthineers, Erlangen, Germany), with sagittal slices of the lumbar spine collected for each patient. These slices were 4 mm thick with a consistent 30 x 30 cm field of view. DWIs were collected at 3 different b-values (v = 50, 400, 800 s/mm^2) using a body coil with a TR of 3000 ms, TE of 93 ms, 6 averages, and a matrix size of 156 x 192. This study was approved by the Institutional Ethics Committee at the Irkutsk Scientific Center of Surgery and Traumatology. Data was de-identified prior to its receipt by the Giers' Laboratory (i.e., identifiable/traceable patient information was removed from DICOMs prior to being delivered) and therefore no Institutional Review Board approval was necessary from Oregon State University.

Data Processing

DWI images were first converted into apparent diffusion coefficient (ADC) maps. The patient imaging data was extracted from the original MRI DICOM file to MATLAB (version 9.5) where it could be accessed for further processing. These data files were processed with a MATLAB program in which the medial slice

level (1, 2, or 3) was selected, and the full lumbar image was cropped down to a single disc by the user (**Figure 2.1**).
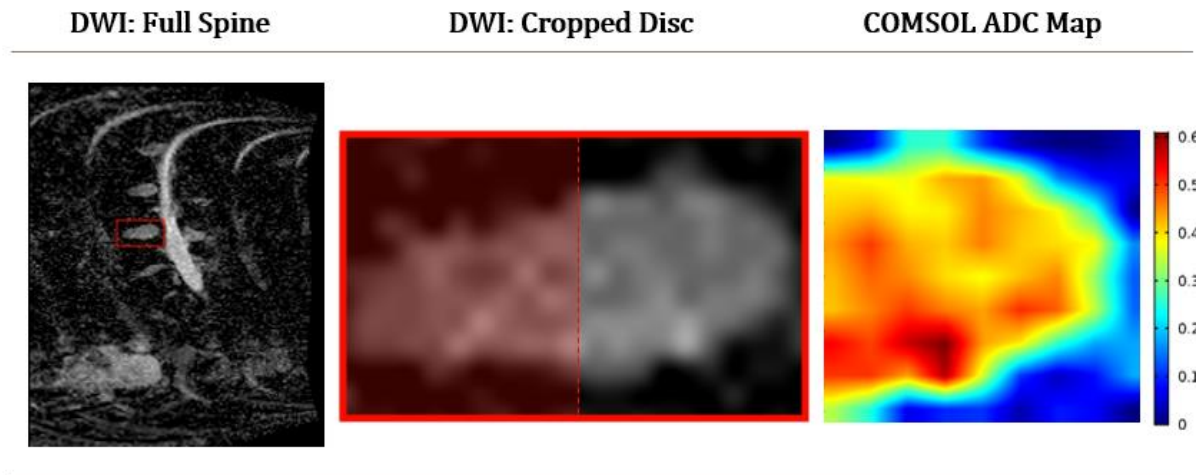
Figure 2.1 – Image processing stages for Patient #1: the diffusion weighted image (DWI) of the whole spine with contrast enhancement (left), the cropped disc segment selected for modeling (middle), and the final cropped disc image as used in COMSOL. Note that the final image is cropped in half, allowing it to be wrapped 360° around the axis of symmetry assigned to the left y-axis, yielding the cylindrical shape that approximates that of a spinal disc (Figure 2.4).

Any negative/infinite points were removed (replaced with a zero), and the ADC values were calculated with the following equation, which is simply a modification of the Stejskal-Tanner equation as established by Le Bihan[124,125]:

$$ADC = \ln \left(\frac{S_0}{S} \right) * \left(\frac{1}{b} \right) \qquad (1)$$

Where S_0 is the fitted value for signal intensity when b = 0, S is the signal intensity provided by the DWI, and b is the gradient value. Diffusion characterization capability increases with the b-value. The maximum ADC value for the disc was noted for scaling purposes (Table 1) before the file was saved (.bmp) for use in COMSOL.

Table 2.1 – Maximum values identified for both the ADC image (determined in MATLAB) and normalized COMSOL image. A ratio of these values was used to convert each image back to the desired ADC scale after being imported into COMSOL as a normalized image. Disc selections are shown in Figure 2.3.
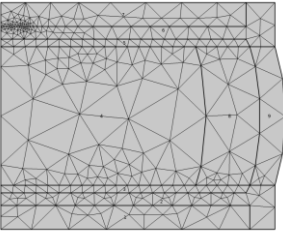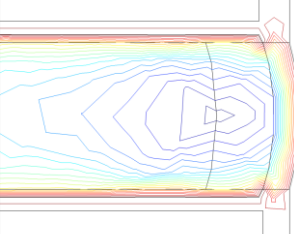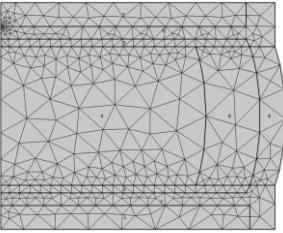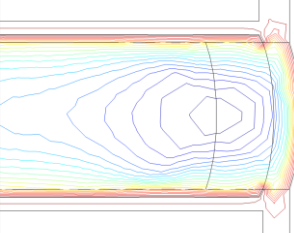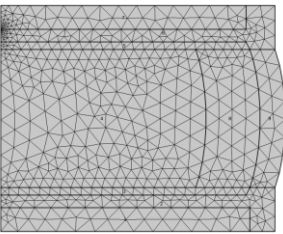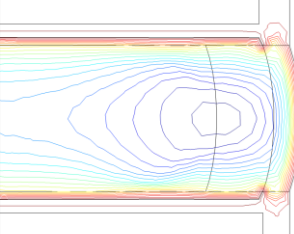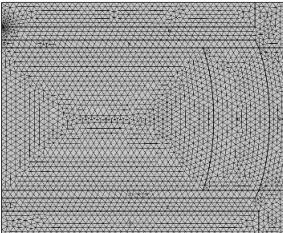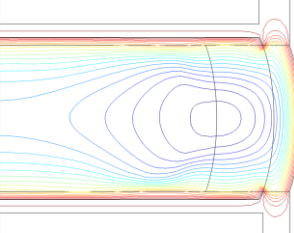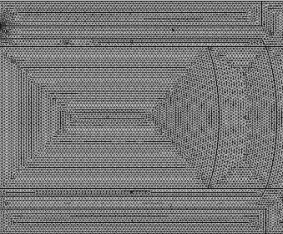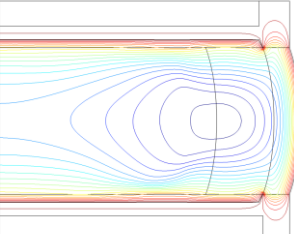
Patient	MATLAB Max Value [m^2/s]	COMSOL Max Value	Disc Level
1	1.92E-03	0.487	L2-L3
2	2.04E-03	0.518	L2-L3
3	1.85E-03	0.468	L1-L2
4	2.18E-03	0.550	L3-L4
5	2.19E-03	0.607	L3-L4

Patient Models

Model Equations, Geometry and Constants

The transport model was developed using COMSOL Multiphysics (version 5.3a). COMSOL offers a variety of mesh types to accommodate a wide range of geometries: four tetrahedra (tets), hexahedra (bricks), triangular prisms (prisms), and pyramids. Within these types, there are also nine pre-set element size settings, ranging from "extremely fine" to "extremely coarse." Sensitivity analysis results for mesh sizing are showcased in **Table 2.2**. The chosen mesh density for this model was "extra fine." Based on the results reported in **Table 2.2**, it is apparent that finer meshes provide a negligible difference in the solution, in fact, the mesh could have produced acceptable results up to two levels coarser. This level of accuracy was made possible by assuming axial symmetry and wrapping the 2D radial slice around the vertical axis to bring it into three dimensions. This is because, as the model complexity increases, coarser meshes are typically required to avoid excessive convergence times. It is also possible to spatially customize mesh density to reduce convergence times, while maintaining the desired level of accuracy in the region of interest. Later versions of this model will likely also require sacrifices in mesh density to reach convergence.

Table 2.2 – COMSOL mesh sensitivity analysis with selected mesh sizes from extremely coarse to extremely fine.

Mesh Sizing	Solution Time	Mesh	Glucose Model Contour
"Extremely Coarse" Max: 0.00747 Min: 0.00113	9 s		
"Coarser" Max: 0.00294 Min: 1.36E-4	9 s		
"Normal" Max: 0.00152 Min: 6.79E-6	10 s		
"Extra Fine" Max: 4.53E-4 Min: 1.7E-6	14 s		
"Extremely Fine" Max: 2.26E-4 Min: 4.53E-7	23 s		

The metabolites of interest were identified as oxygen, glucose, and lactic acid. The primary mechanism for IVD cells to gain energy is through glycolysis;[58] during glycolysis, glucose molecules are chemically cleaved into two lactate molecules. In diffusion-limited systems, this metabolic process can lead to a buildup of lactate (lactic acid) inside the tissue, causing a drop in pH. This relationship between metabolism and pH is used to couple the concentration model equations for metabolites in the disc.[17] The primary equations are based on Fick's Law for diffusion and the general transport equation:

$$\frac{dC_A}{dt} = D_{AB}\left[\frac{1}{r}\frac{d}{dr}\left(r\frac{dC_A}{dr}\right) + \frac{1}{r^2}\frac{d^2C_A}{d\theta^2} + \frac{d^2C_A}{dz^2}\right] + \dot{R}_A^v \qquad (2)$$

Where R is in $\left[\frac{mol}{m^3}\right]$ per hour (positive for production, and negative for consumption); C is the solute concentration (% for oxygen and $\left[\frac{mol}{m^3}\right]$ for glucose and lactate); and D is the diffusion coefficient for the solute in the given solvent. Values for oxygen were originally given in kPa and converted to concentration using Henry's law. The maximum value for dissolved O_2 was determined to be $5.30 * 10^{-2}\left[\frac{mol}{s}\right]$ based on literature values for blood oxygen concentration.[60] This value was used to scale oxygen concentration in model equations such that oxygen was reported in units of % saturation. A summary of all the variables used in the COMSOL model is provided in **Table A3.2** of **Appendix 3**. The reaction terms as they were entered into COMSOL are provided in **Tables A3.3-A3.5** of **Appendix 3**, briefly:

For lactate generation:

$$log(Lactate\ Generation) = -2.47 + 0.93 * pH + 0.16 * O_2 - 0.0058 * O_2{}^2 \qquad (3)$$

Or:

$$Lactate\ Generation = e^{-2.47 + 0.93*pH + 0.16*O_2 - 0.0058*O_2{}^2} \qquad (4)$$

For oxygen consumption:

$$Oxygen\ Consumption = \frac{7.28*O_2*(pH-4.95)}{1.46 + O_2 + 4.03*(pH-4.95)} \qquad (5)$$

For glucose consumption, at any given point the consumption rate of glucose will be half that of the production rate of lactic acid (via the mechanism of glycolysis):

$$Glucose\ Consumption = \frac{1}{2}\ Lactate\ Generation \qquad (6)$$

The distinct tissue types in and around disc each have specific production/consumption rates for each solute, scaled according to the cell density and water volume fraction of the given tissue (**Table 2.3**). The equations outlined above were also developed specifically for the NP. To apply them in the remaining areas of the disc, the equations were necessarily scaled using the ratio between the number of cells in the tissue and the number of cells in the NP.[126] This ratio was included in the constants for scaling and unit conversion which were calculated for each tissue region in the model. A diagram of the tissue regions included in the model is shown in **Figure A2.3** of **Appendix 2**.

Region of Interest	Cell Density $\left[\dfrac{million\ cells}{mm^3}\right]$	Water Volume Fraction % (ε)	Constant for Unit Conversion	Variable Assignment (COMSOL)
CEP	0.004	60	1.56E-05	C_CEP
NP	0.012	80	1.11E-06	C_NP
IA	0.006	73	2.50E-06	C_IA
OA	0.015	66	1.00E-05	C_OA

Table 2.3 – Summary of cell density and water volume for each tissue region, including the final unit conversion constants which combines appropriate ratios of cell density, and conversions from *nmol* to *mol*, mm^3 to m^3 and *h* to *s*. Water volume fractions were used when converting oxygen concentration equations from units of kPa to %. IA and OA represent the inner and outer regions of the annulus fibrosis.

Boundary Conditions

In addition to the behavior of solutes in the bulk tissue, the model also accounts for the behavior of solutes at tissue boundaries. Three distinct boundaries were identified (**Figure 2.2**): the interface between the BEP and CEP (BC1), the interface between external tissues of the lumbar region and the OA (BC2), and the additional non-interface (no contact assumed) between the edges of the OA and the BEP (BC3). Boundary group 3 was assumed to be no-flux in order to correct for structural simplifications made when defining

the disc geometry. For all other boundaries, a fraction of the external concentration was assumed to cross

the boundary based on the relative conductivity in the tissue (**Table 2.4**).[63]
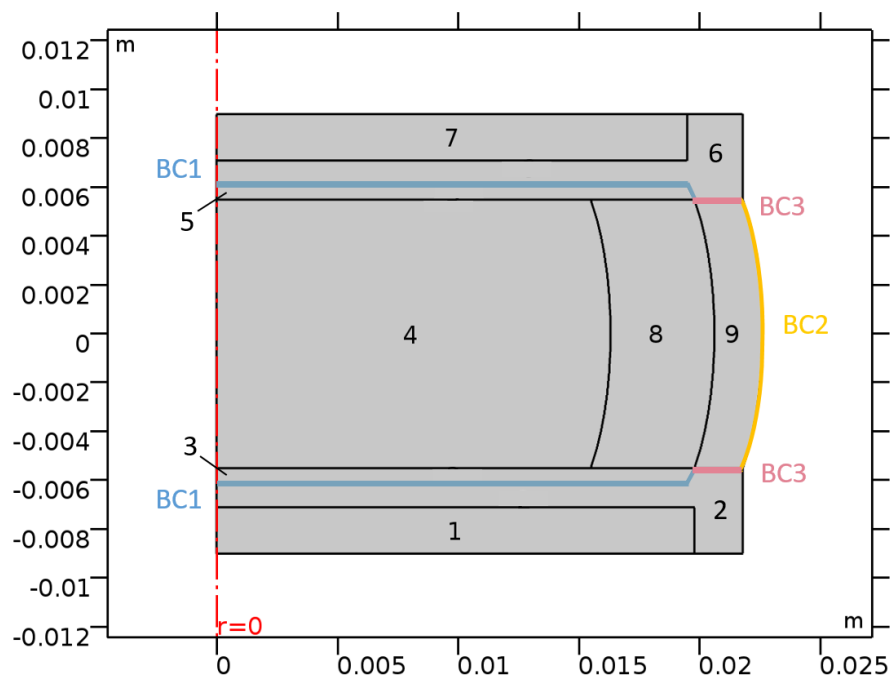
Figure 2.2 – Disc geometry model including regions segmented for cancellous bone (1 & 7), cortical bone (2 & 6), the CEP (3 & 5), OA and IA (9 & 8), and the NP symmetry (r=0) for the 2D axisymmetric model is shown in red. The 2D model will be wrapped around the y-axis, yielding a short cylinder (shown in Figure). Lengths are given in meters [*m*].

Furthermore, though the model is designed to incorporate patient data, this functionality is limited

specifically to the NP region, all other regions (including the CEP, IA and OA) rely on previously determined

values for diffusion (**Table 2.4**).[60] Due to a lack of data available for diffusion through cortical and

cancellous bone, it was assumed that diffusion in the denser cortical bone is an order of magnitude lower

than the cartilaginous endplate, while in the spongy cancellous bone, diffusion is an order of magnitude

higher. This is a limitation of the current model that could be addressed in future work. Proper

characterization of these properties is important due to the influence of the BEP on disc degeneration. As

the disc degrades, one would likely see comparable changes to transport in the BEP as in the IVD. In fact,

extreme changes in BEP diffusion properties could potentially be seen as a precursor to IVD degeneration.

Further characterization in this area is necessary to achieve model validation.

Table 2.4 – Diffusion coefficients (D) and boundary conditions (BC) for nutrients and metabolites in various regions of the disc as defined in Soukane et al, 2007.[126] $BC_1 = 0.8\ C_0$ for oxygen and lactate, $BC_1 = 0.71\ C_0$ for glucose, and $BC_2 = 0.9\ C_0$, where $C_{0,\ Oxygen} = 6.4$ kPa, $C_{0,\ Glucose} = 5.6$ nmol/mm3, and $C_{0,\ Lactate} = 1.0$ nmol/mm3. Boundary 3 was assigned no-flux, as the two structures do not interact this way in the human body, this arrangement was merely a simplification for modeling purposes.

Region of Interest	Oxygen		Lactic Acid		Glucose	
	D $\left[\frac{m^2}{s}\right]$	BC $[kPa]$	D $\left[\frac{m^2}{s}\right]$	BC $\left[\frac{mol}{m^3}\right]$	D $\left[\frac{m^2}{s}\right]$	BC $\left[\frac{mol}{m^3}\right]$
CEP	7.806E-10	5.1	3.139E-10	0.8	2.111E-10	4
IA	1.156E-09	-	4.667E-10	-	3.139E-10	-
OA	9.444E-10	5.8	3.806E-10	0.9	2.556E-10	5

For the NP region, the data provides a value for water diffusion $\left[\frac{m^2}{s}\right]$ in the tissue. A method for calculating hindered solute diffusion in solvent-filled pores has been established by Renkin:[127]

$$\frac{D_{Ae}}{D_{AB}^0} = F_1(\varphi)F_2(\varphi)$$

This equation describes the diffusion of a solute molecule (species A) through a tiny capillary pore filled with a liquid solvent (species B). As size of the molecule increases, the diffusive transport of the solute through the solvent is hindered by the presence of the pore, specifically the pore wall. This hindrance is modeled with two correction factors, F_1 and F_2, which are both functions of the reduced pore diameter (φ), and are theoretically bounded by 0 and 1:

$$\varphi = \frac{d_s}{d_{pore}} = \frac{solute\ molecular\ diameter}{pore\ diameter}$$

The correction factor $F_1(\varphi)$ is known as the stearic partition coefficient, it is based on geometric arguments for stearic exclusion:

$$F_1(\varphi) = \frac{flux\ area\ avaiable\ to\ solute}{total\ flux\ area} = \frac{\pi(d_{pore} - d_s)}{\pi d_{pore}^2} = (1 - \varphi)^2$$

The correction factor $F_2(\varphi)$ is known as the hydrodynamic hindrance factor. It is based on a number of hydrodynamic calculations, including the hindered Brownian motion of the solute within the solvent-filled pore. Renkin developed the following relationship for $F_2(\varphi)$, assuming the solute is a rigid sphere diffusing through a straight cylindrical pore:

$$F_2(\varphi) = 1 - 2.104\varphi + 2.09\varphi^3 = 0.95\varphi^5$$

Based on this, the ADC value for a given solute was scaled based on a ratio of literature values for diffusion of the solute in water, and the diffusion of water in water:

$$D_{W/T}\left[\frac{m^2}{s}\right] * \frac{D_{S/W}\left[\frac{m^2}{s}\right]}{D_{W/W}\left[\frac{m^2}{s}\right]} = D_{W/T}\left[\frac{m^2}{s}\right] * D_{S/W}\left[\frac{m^2}{s}\right] = D_{S/T}\left[\frac{m^2}{s}\right]$$

This relationship was determined based on the assumption that all four solutes (O2, glucose, lactate and water) were sufficiently small (on the scale of 100-1000 pm) relative to the pore to approximate $F_1(\varphi)$ and $F_2(\varphi)$ as the same across the solutes. This assumption allows for the following simplification:

$$D_{S/T} = \left[D_{W/T}\right] * \left(\frac{D_{S/W}}{D_{W/W}}\right) = \left[D_{W/W} * F_1(\varphi) * F_2(\varphi)\right] * \left(\frac{D_{S/W}}{D_{W/W}}\right) = D_{S/W} * F_1(\varphi) * F_2(\varphi)$$

Assuming the tissue is sufficiently hydrated, the diffusion of water in the tissue can be modeled as the hindered self-diffusion of water through a solvent filled pore, in which the constants $F_1(\varphi)$ and $F_2(\varphi)$ are already accounted for in the ADC. Accounting for the relative molecule size would require characterization of the specific tissue pore sizes, which is beyond the scope of this project. Using this method, scaling constants were generated for each solute (**Table 2.5**), such that the value determined for the diffusion of water in the patient's tissue could be converted to a value for the diffusion of glucose, lactate or oxygen in the tissue. See Appendix 3 for a summary of the constants and equations as they were inserted into COMSOL, including specific

Table 2.5 – ADC conversion from water in tissue to nutrient/ metabolite in tissue.

Solute	$D\left[\frac{m^2}{s}\right]$
$D_{W/W}$	3.05E-9[128]
$D_{G/W}$	9.17E-10[54]
$D_{L/W}$	1.39E-09[54]
$D_{O/W}$	3.00E-09[54]
$D_{G/W}$	0.30
$D_{L/W}$	0.46
$D_{O/W}$	0.98

formatting and variable assignments. Initial values for concentration of solutes in each region of the disc were determined from literature and assigned accordingly (**Table 2.6**). Briefly, peak values for nutrients were applied to the boney endplate which have direct blood supply, and the minimum values were assigned at the center of the disc where diffusion limitations are typically the most pronounced.

Table 2.6 – Initial conditions for concentration of metabolites in various areas of the disc (CEP, AF and NP) and adjacent tissues (cortical and cancellous bone).

	Blood	Cort. Bone	Canc. Bone	CEP	AF	NP	Disc Center
Lactate $\left[\frac{mol}{m^3}\right]$		1.00			5.00		10.00
Glucose $\left[\frac{mol}{m^3}\right]$		5.56			2.80		0.00
Oxygen $[kPa]$		6.40			3.55		0.70
Oxygen $\left[\frac{mol}{m^3}\right]$		0.05			0.01		0.01

Results

With the methods described previously, the diffusion behavior within a lumbar disc (Pfirrmann grade 2) was modeled for 5 patients. Disc selections are shown in **Figure 2.3**. An example of a typical 3D rendered model is shown in **Figure 2.4**. This model was generated by wrapping the 2D models of solute diffusion (**Figure 2.5**) around the y-axis of symmetry.

Figure 2.3 – T2 images for patients 1-5. Discs selected for modeling are highlighted in red.
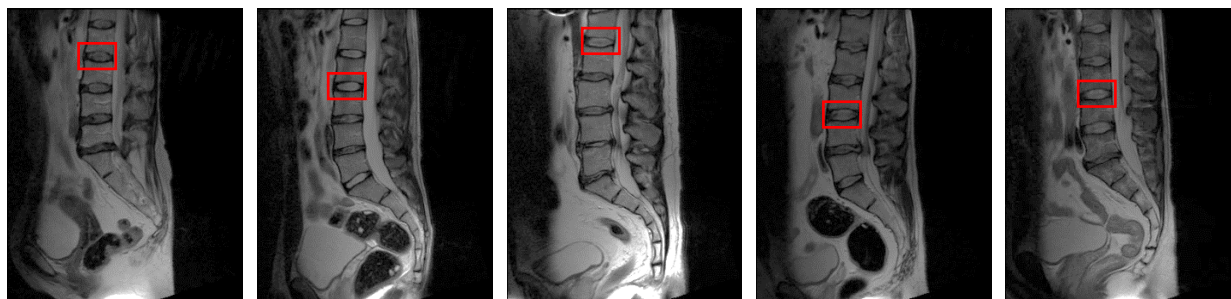
The models showcased in **Figures 2.4** and **2.5** represent the steady state distribution of nutrients and metabolites in the disc based on the patient's specific nutrient diffusivities. All models were run out to one week (t = 10,080 min) with no discernable visual changes in the solute distribution within the disc

towards the 50 hour mark. The glucose and oxygen models show a zone of low concentration which reaches a minimum at the interface between the IA and NP, meanwhile the lactic acid model shows peak concentrations in the same area.

Glucose	Lactic Acid	Oxygen
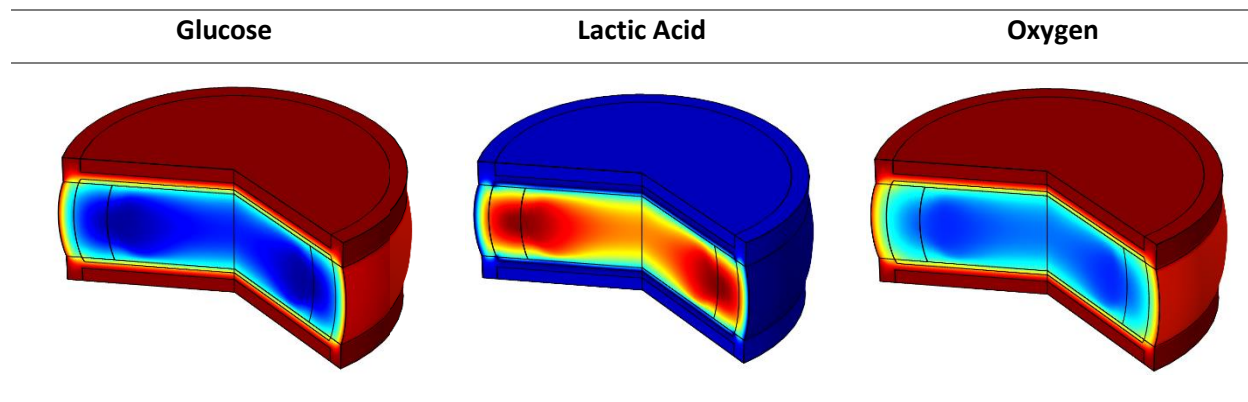
Figure 2.4 – Characteristic 3D models for glucose, lactic acid and oxygen distribution within the disc for Patient #1. These were generated by wrapping the 2D models of nutrient/metabolite concentration shown in Figure 1-3 around the y-axis of symmetry. For individual concentration scales see Figure 2.5.

Of greater interest is the local variation between patients: though general trends across all 5 patients are consistent with prior knowledge, the specific trends of each patient are unique. When comparing the specific trends for each solute across all 5 patients, distinct patterns are discernable, indicating that the individual physiological conditions of each patient's discs makes an important difference to the metabolite gradients, even among discs of the same Pfirrmann grade. Specifically, the shape of the gradients, the specific size and location of the "dead zones", and the magnitude of nutrient/metabolite extrema are markedly different between patients. Between these models, the only point of variance was the diffusion maps applied for the nucleus area, the rest of the model settings and parameters were uniform between patients.

25
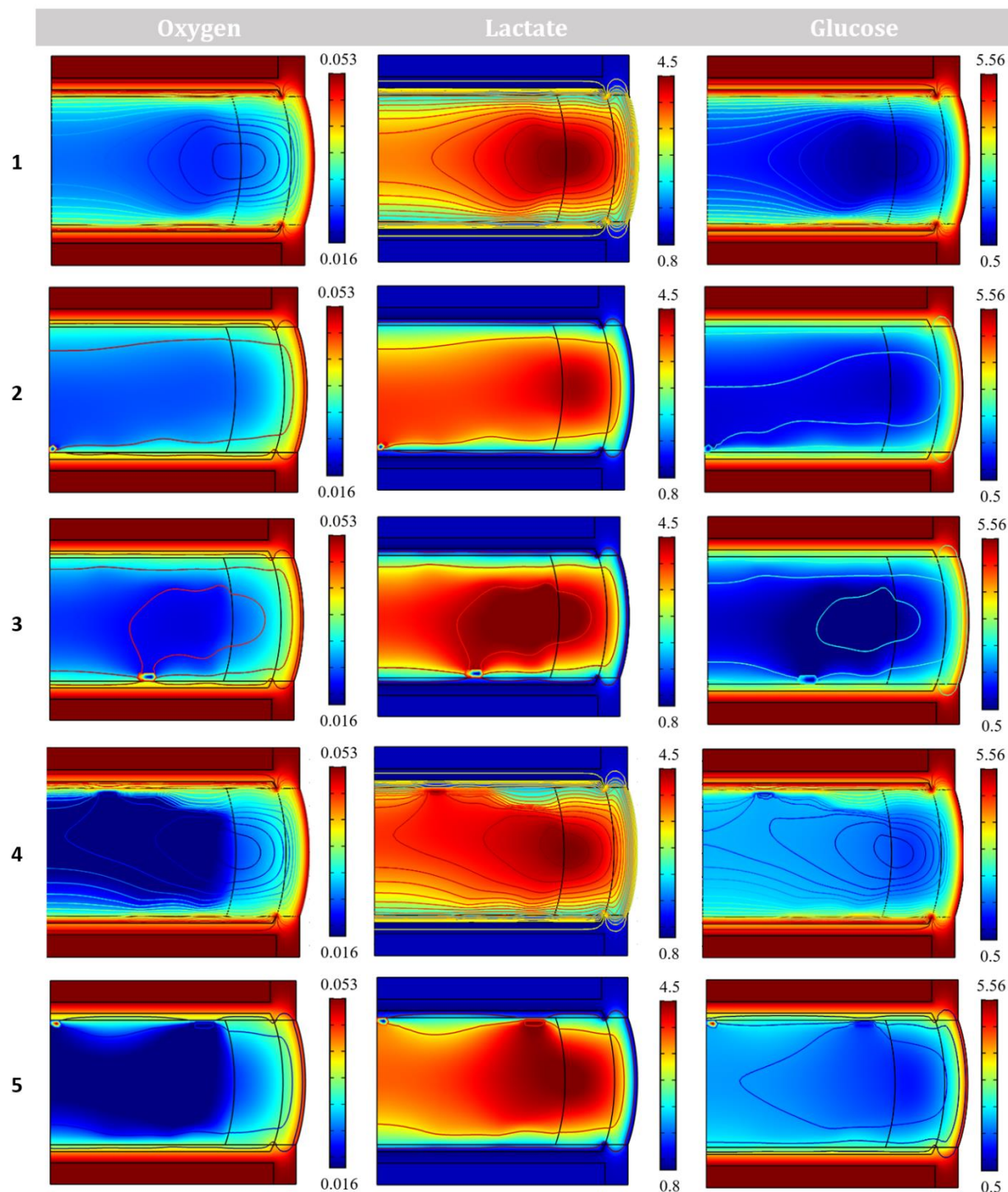
Figure 2.5 – Characteristic distribution of oxygen (left), lactate (middle) and glucose (right) within the disc for patients 1-5. For oxygen, the scale ranges from a minimum of 0.016 [mol/m^3] (deep blue) to a maximum of 0.053 [mol/m^3] (deep red). For lactate, the scale ranges from a minimum of 0.5 [mol/m^3] (deep blue) to a maximum of 5.56 [mol/m^3] (deep red). For glucose, the scale ranges from a minimum of 0.8 [mol/m^3] (deep blue) to a maximum of 4.5 [mol/m^3] (deep red).

Discussion

The general model behavior agrees with that of previous investigations on general solute diffusion trends,[60,126,129] and also makes logical sense based on what is known about the structure of the disc. Namely, that the AF is a dense, fibrous tissue with slow diffusion speeds, while the NP is a highly saturated tissue with relatively fast diffusion speeds. This means that solutes diffusing radially (both inwards and outwards) experience a bottleneck at the AF but can diffuse freely within the nucleus. The inner AF region at the midline of the disc also contends with the longest diffusion distances from either endplate. In this diffusion-limited zone, a lack of sufficient diffusion leads to a critical deficit of nutrients, and a toxic buildup of metabolic products (lactate). According to the model results, the pH in these areas is at a minimum, which can cause metabolic suppression and cell death at certain levels.[60,129] Specifically, cell death is significant when pH drops to 6.2 or below.[130] Likewise, IVD cell death has been shown to initiate at glucose levels below 0.5 mM, and at 0.2 mM all cells die in 3 days.[64] The patient-specific variation demonstrated by the present model supports the hypothesis that degeneration grade alone is insufficient to predict the nutrient environment in the disc, particularly the presence, location and magnitude of these "dead zones." Accurate localization of these zones of cell death could prove vital for novel IVD therapies which aim to either increase cell activity or cell count in the disc.

As previously mentioned, a major limitation of current treatments for LBP is simply that the treatments are aimed at treating the symptoms rather than the root cause of LBP, which many studies indicate may be degeneration of the IVD.[5–8] Research into novel treatments for LBP has increasingly focused on development of biologic therapies for the disc to halt or even reverse tissue degeneration. Unfortunately, the interplay between increasing the cell activity/ density in the disc and subsequent changes to nutrient availability is frequently overlooked during implementation of these strategies, and as a result their success has been rather limited. In particular, high variability in cell dosaging schemes prevents the true efficacy and relative success of these therapies from being assessed; a recent review of IVD cell injection therapies reported cell concentrations ranging from 1 to 121 million cells. [131] The results of the current

study further emphasize the importance of specific and tailored treatments; IVD-specific nutrient availability must be accounted for to prevent nutrient demands from exceeding the capacity of the system and causing a cell population collapse. Unfortunately, the optimal number of cells to inject in order to produce a desired effect is currently unknown.[132] Based on preliminary results presented here, we anticipate future iterations of this model could prove extremely useful for development of standardized specific dosing schemes for biological treatments of IVD degeneration.

However, the results shown in **Figure 2.5** also demonstrate some key limitations of the current modeling scheme which should be addressed in future iterations. Visible in **Figure 2.5** are computational "nodes" which indicate failure of the model to accommodate certain areas of data, or an issue of compatibility of the cropped image with the generic model geometry. This is likely the product of pixel limitations (lower resolution) and limited patient data incorporated into only one region of the model. Future work should ensure collection of higher resolution images to facilitate better compatibility between model geometries and diffusion maps. Note that this study used images from a 1.5 T MRI, leaving much room for improvement in this area. Future work should also focus on generating a geometry directly from the patient's morphology as captured by the MRI, rather than trying to match a patient's disc to a generic, pre-made geometry. In addition to causing nodes from geometry miss-match, the current model is only valid for patients with discs Pfirrmann grade 2 or below. This is because, at higher levels of degradation, relatively extreme morphological changes typically start manifesting, causing incompatibility with the rigid COMSOL geometry used here. This only heightens the need for alternative geometry generation strategies, which would increase both model utility and accuracy, and save time by eliminating the need to make the model geometry separately. Additionally, this model incorporates patient data only into the NP region. This is because this region is the one best captured by DWI. However, incorporating data from the other regions of the disc (IA and OA) could prove extremely valuable, particularly in the case of disc rupture, or endplate calcification. Future work should explore methods of collecting diffusivity data from

other regions of the disc. This process could be part of a larger effort to validate model predictions through disc tissue biopsy and analysis in animal models.

The model also assumes a fixed cell density in each region based on values identified in previous work for cell concentration in various disc tissues. The solution therefore does not account for how cell death due to "dead zones" of nutrients would affect the nutrient distribution within the disc. This can also cause issues if the model is put to extremes of concentrations or cell density, as shown in **Figure 2.6** and tabulated in **Table A3.6** of **Appendix 3** which shows predicted concentrations of glucose becoming negative, which is not physiologically possible. Future work should attempt to model the dynamic changes in cell density associated with patient specific nutrient gradients and degradation. Models have already been developed which account for cell viability changes using a step function based on the thresholds for cell death outlined previously.[133] This should be a relatively straightforward addition to the model, though it will likely impact the ability of the model to reach steady state. Regardless of the extent to which these various limitations hinder the specific accuracy of these models, these results demonstrate the importance of the specific diffusive properties and nutrient limitations within the disc, and how slight changes can impact the disc microenvironment.

NP Cell Density $[10^6 \frac{cells}{m^3}]$	Glucose	Lactate	Oxygen
4.00E+03			
2.00E+06			
4.00E+06			
6.00E+06			
8.00E+06			
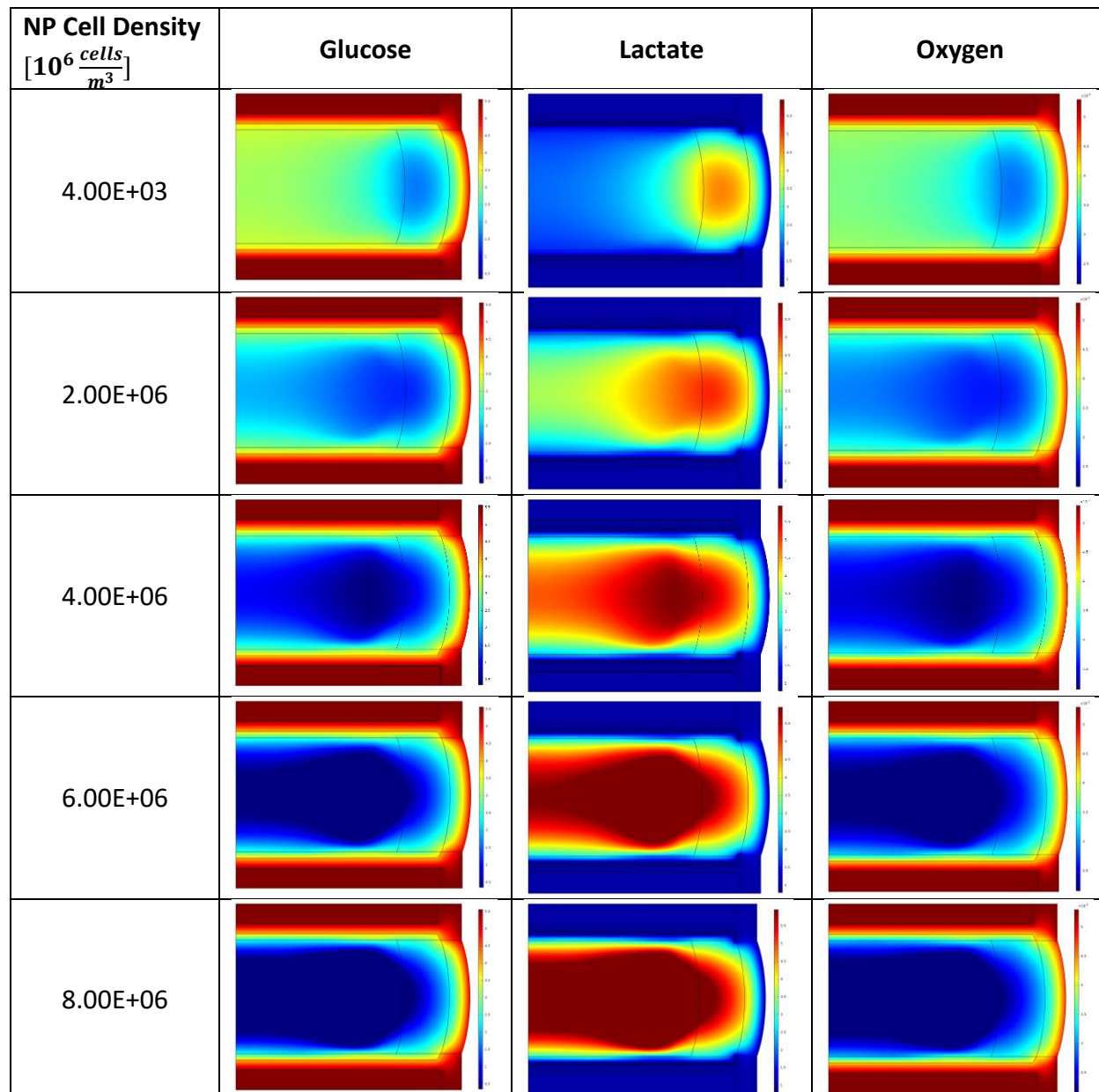
Figure 2.6 – Impact of changing NP cell density on nutrient distribution in the disc.

Conclusions

This work describes a method for incorporating patient data into a nutrient transport model of the intervertebral disc. Results show distinct diffusion behavior between patients, even within discs of the same Pfirrmann grade. The importance of the distinct disc morphologies and physiological environments of each patient to the diffusion gradients in the disc is readily apparent. Patient-specific models could allow clinicians to further personalize treatments to the patient. Pending further development, this model

could allow clinicians to account for the impact of increasing cell activity or density in a nutrient-starved environment, namely in the generation of dead zones. This model could be used as a tool to look for critical concentrations and pH's in the patient's discs (i.e. levels below which cells cannot survive). If levels are already low enough to indicate cell death, these patients would likely not be good candidates for biological therapies. For patients without a dead zone, the model could be used to determine proper dosing for various therapies via iteratively increasing cell concentration/activity until the patient develops a dead zone. This functionality indicates that patient-specific models could prove valuable in a clinical setting when predicting patient outcomes or treatment options.

Future Work

The new version of the model recently developed by our group has addressed some of limitations of the model presented here, mainly by eliminating the necessity for a rigid, generic geometry.[134] This allows for the disc's unique geometry to be preserved, creating an even more specific and realistic model for the analysis of discs of different morphologies and degeneration grades. This was accomplished by creating a generic square "sandbox" which was then set to physiological concentrations of glucose, oxygen and lactate, acting as a well-mixed container in which solute transport can take place. The segmented disc was then placed inside of this well-mixed container and allowed to equilibrate. The resulting concentration gradients of glucose, lactate and oxygen are shown in **Figure 2.7**. This is reflective of the disc's nutrient exchange behavior with the blood, as vasculature is present at both the endplates and the outer AF, allowing for exchange between the blood and disc microenvironment. In the new model, most discs demonstrated solute concentration extrema (i.e. peak lactate and minimum glucose and oxygen) at the boundary between the AF and NP, which is in agreement both with the previous version of the model and with the literature. Beyond this, the model shows much improved behavior: there are no "nodes" and the "sandbox" technique enable the patient's specific geometry to be preserved. This is especially important for cases of advanced degeneration (see the Grade 5 disc below), or abnormal geometry (e.g. extremely tall discs), which can cause heightened nutrient limitations or abnormal transport behavior. This model

doesn't incorporate a cell death model, however, which is the next priority after this version of the model

undergoes validation testing.
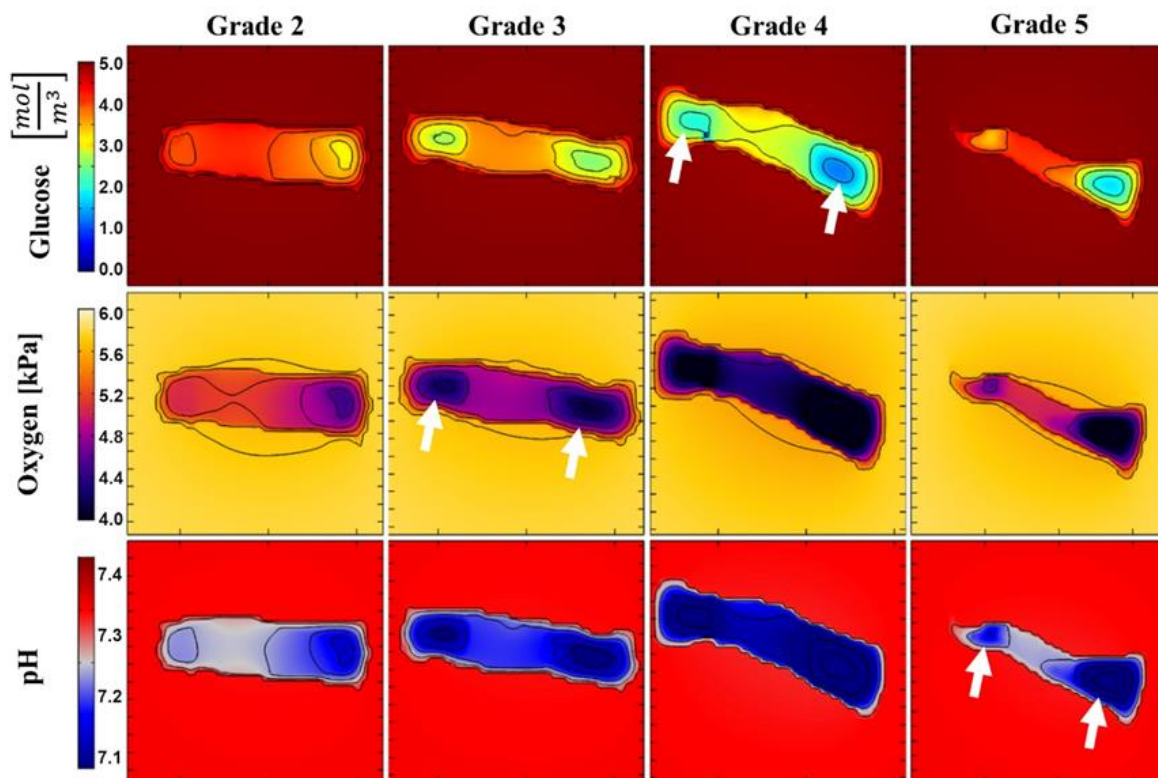
Figure 2.7 –Examples of solute and pH distribution models of discs with different degeneration grades. The lowest levels of nutrients and the highest levels of acidity appear at the inner AF region in most discs (marked with white arrows).

Chapter 3: MRI

Introduction

Clinically, IVD degeneration is often measured qualitatively via visual inspection of MRI images. Assessment of spinal pathology is typically performed by both the radiologist and the surgeon, and may include assessment of degeneration grade[67] in addition to evaluation for other pathologies. Unfortunately, certain tissue properties can be difficult or impossible to discern via traditional clinical imaging methods (i.e. T1-weighted ($T1_w$) and T2-weighted ($T2_w$) imaging) which may be essential for assessment of disc herniations. For example, though $T1_w$ images can be used to confirm disc herniation, the size of the herniation is often underestimated because the signal of the disc tissue and spinal cord are difficult to distinguish with this modality.[135] $T2_w$ imaging is currently the gold standard for localization of lumbar disc herniations. However, as the disc degenerates the NP tissue begins to visually resemble AF in this modality, making it difficult to determine which tissue has herniated.

As previously established, modalities like diffusion-weighted imaging (DWI) might offer additional information to improve patient evaluation and treatment. DWI detects the signal associated with the self-diffusion of water molecules in the tissue[136] and can be used to generate apparent diffusion coefficient maps (ADC maps) which quantify this water movement as diffusion coefficients. These ADC maps can be used in several ways, including as an overlay for $T2_w$ images to enable better localization of the NP during visual inspection,[123] or to extract the diffusive properties of the NP for use in computational models of the IVD. DWI has great potential to improve NP evaluation, but its accuracy and sensitivity relative to the standard clinical imaging modalities remains to be quantified, this is the focus of the current work.

In this investigation, image processing techniques were used to quantitatively compare NP properties and morphology as determined by ADC and $T2_w$ imaging. Other groups have previously evaluated discs using quantitative methods,[80,137–140] and even compared these results to ADC,[141] however the metric of performance is often in agreement with the Pfirrmann grade. Though Pfirrmann grade analysis is included in this work, it is not the end point of validation for this project. As a metric of validation, comparison to

the Pfirrmann grade alone leaves much to be desired because the Pfirrmann grade is neither quantitative nor an objective method of assessment for the disc. And, as previously established by our patient-specific nutrient modeling work, the disc microenvironment can vary greatly even between discs of the same Pfirrmann grade. The long-term goal of the current work is to compare the results of imaging studies directly to tissue samples to determine which modality is truly best at visualizing the tissue. For this we propose an animal model, specifically bovine tails. Though this experiment is beyond the scope of the work presented here, the procedure is currently being developed. Further details about the animal model can be found in the future work section of this chapter.

Furthermore, due to the inherent variability of MR signal intensity, data is frequently not translatable between studies. This variability can come from a variety of sources, including the specific imaging settings (pulse sequence, spacing, patient-specific tissue properties etc.) or just the MRI machines themselves, which can vary in both strength or design.[142] In the present work, an internal standard was used to correct for the effects of MRI hardware and software inconsistencies. Internal standards are intensity measurements taken of a tissue that should have nearly identical pixel intensity across all patients which can be used to normalize data. Spinal fluid (SF) is a common internal standard used in image processing of the spine,[143–146] and is the internal standard used in the current work. We did this both to enable better comparisons within our own dataset, and to enable wider utility of this data for other research groups.

Materials & Methods

Data Collection and ROI Development

MR sagittal $T1_w$, $T2_w$ and DW images were obtained for the lumbar spine of 47 patients admitted for spinal surgery at the Irkutsk Scientific Center of Surgery and Traumatology. **Table 3.1** summarizes patient demographic information. De-identified image data was extracted from the original MRI DICOM file to MATLAB (version 9.5) where it could be accessed for further processing. These data files were processed with a MATLAB program in which the image slice depth was selected, and DWI was converted to ADC with

the following equation, which is simply a modification of the Stejskal-Tanner equation as established by

Le Bihan:[124,125]

$$ADC = \ln\left(\frac{S_0}{S}\right) * \left(\frac{1}{b}\right) \qquad (1)$$

Where S_0 is the fitted value for signal intensity when $b = 0$, S is the signal intensity provided by the DWI, and b is the gradient value. Diffusion characterization capability increases with the b-value. Manual IVD segmentation was performed for lumbar levels L3/L4, L4/L5, and L5/S1 using three mid-sagittal slices from each patient in Materialise Mimics (**Figure 3.1**). Levels L3/L4-L5/S1 were used because they were consistently visible on all patients, enabling direct comparison. First, $T1_w$ images were used to locate and segment the endplates of each disc; $T1_w$ provided better distinction between the endplate and the rest of the vertebral body than $T2_w$ images or ADC maps. These masks were transferred to the $T2_w$ images and used to segment the whole IVD structure. The cross-sectional area and centroid of the IVD was extracted for each level at this stage. The whole-IVD masks were then copied to the corresponding ADC maps and used to perform NP segmentation via histogram-based thresholding for both modalities in MATLAB.

Table 3.1 – Key demographics and characteristics of the patient population.

Patient Characteristics:	
Total number of patients, n	47
Sex:	
Male, n	43
Female, n	4
Age:	
Range, years	22-57
Mean, years	41.1 ± 9.0
IVD Pfirrmann Grade:	
Grade 1, n	0
Grade 2, n	29
Grade 3, n	65
Grade 4, n	39
Grade 5, n	8
Total IVDs assessed, n	141
Types of IVD herniation:	
Protrusion, n	29
Extrusion, n	21
Sequestration, n	2
Level of IVD herniation:	
L3-4, n	4
L4-5, n	19
L5-S1, n	29
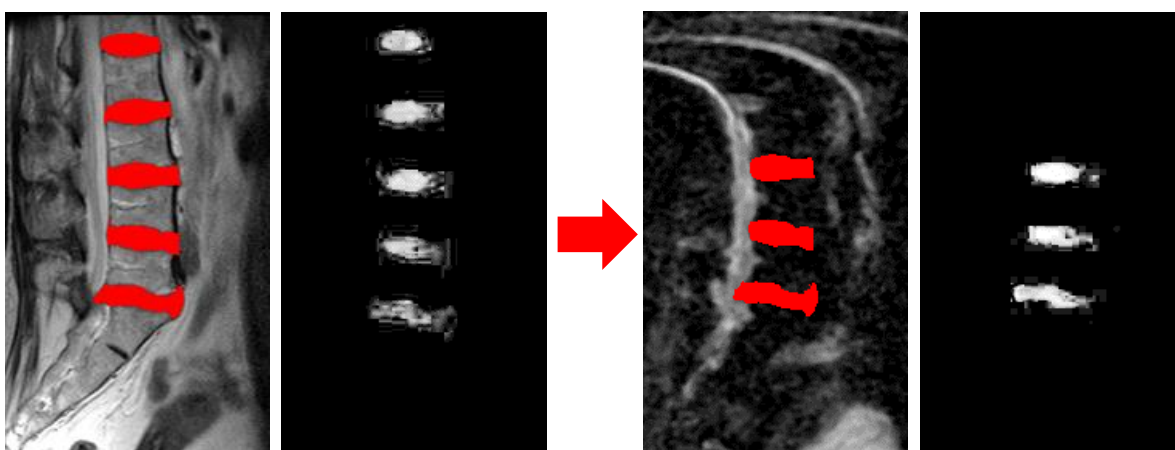
Figure 3.1 – Example of manual IVD segmentation of T2w (left) and ADC (right).

Histogram-Based Thresholding

Histogram-based thresholding is an established image processing technique which relies on the tissue-specific pixel intensity exhibited by different tissues (due to the specific physical properties of those tissues) to varying degrees of contrast in different MRI imaging modalities. In this case, the primary substructures of the IVD give off distinct signal intensities which can be segmented via thresholding. Specifically, a multi-peak Gaussian distribution was fit to the image histogram, and the resulting peaks were separated to differentiate the substructures (**Figure 3.2**).[138]
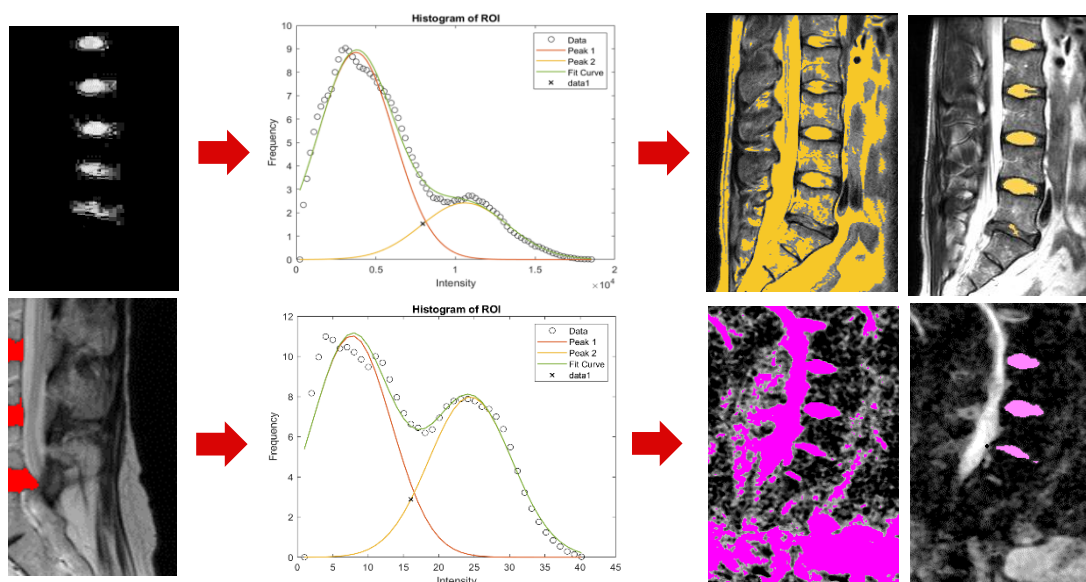
Figure 3.2 – Demonstration of separation of NP and AF/EP using histogram thresholding in MATLAB.

The specific process varies between modalities. In the case of $T2_w$ imaging, all tissues are present in the image, if not always readily differentiable upon visual inspection. In general, the AF has lower overall signal intensity than the NP, so in segmented $T2_w$ images there are typically two major peaks found in the histogram: one for the AF (lower) and one for the NP (higher). In DWI/ADC however, the NP is the only tissue in the disc saturated enough to give off a detectable signal, therefore there is typically a peak for the NP and a second peak for the noise in the background. However, these rules are not absolute. For example, advanced NP degeneration can cause $T2_w$ images to have only one peak. The standard deviation of the NP peak in both modalities was used to calculate a minimum threshold value for pixel intensity of the nucleus, below which the pixel was determined to belong to a different tissue, like the annulus fibrosis, or the background, both of which can be negated. Additionally, the relative position of these peaks has also been correlated with degeneration grade because degeneration changes tissue properties which in turn alters MRI signal intensity, both in $T2_w$ images and ADC maps (**Figure 3.3**). These correlations suggest that histogram thresholding should also be a useful tool to evaluate degeneration.
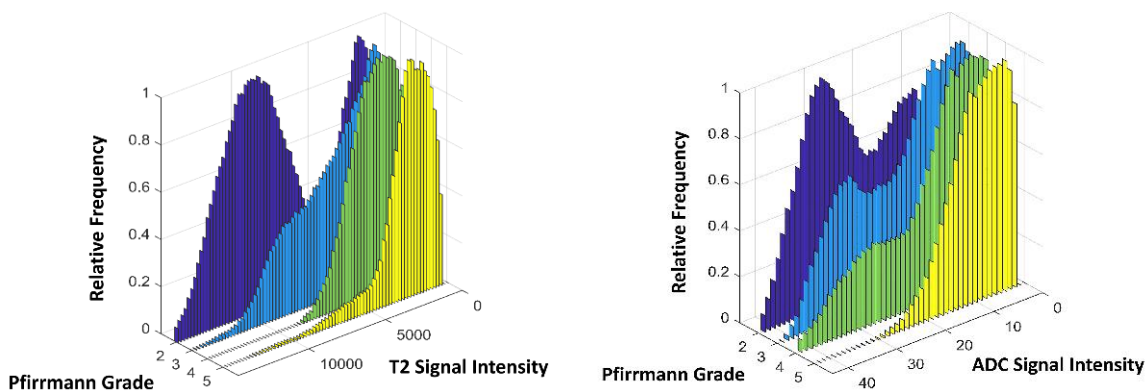
Figure 3.3 – Demonstration of histogram shift with degeneration grade in T2w images (left) and ADC maps (right).

NP Area and Intensity Measurements

Following thresholding, the segmented masks of the NP were used to extract key properties including NP

intensity and NP area via processing in MATLAB. First, the NP threshold mask was used to "cut out" the

designated portion of the original image via a series of binary image manipulations, such that the only

part of the image remaining was the NP. The remaining area was converted to black. Each segmented NP

was then separated by lumbar level for individual analysis of sagittal cross-sectional area and width. The

NP dimensions and disc centroids were used to make a region of interest (ROI) of uniform area located at

the centroid of the disc to extract values for average NP pixel intensity. Values for spinal fluid intensity

were also collected as the internal standard for later use in normalizing the average NP intensity values.

Figure 3.4 shows a summary of this entire process from patient imaging to NP area and pixel intensity

measurements.
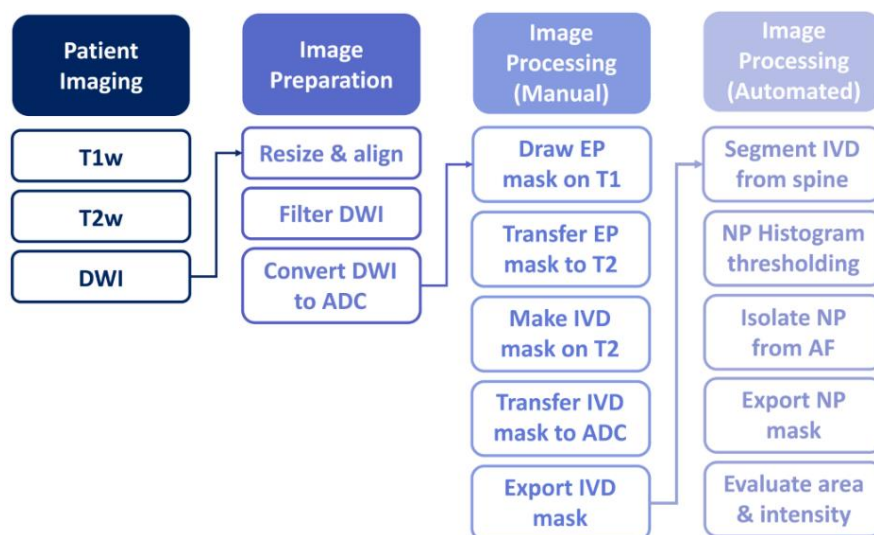
Figure 3.4 – Image processing protocol overview.

Results

The average NP area was calculated for each disc in both T2$_w$ images and ADC maps. The results for all

levels are shown plotted against Pfirrmann Grade in **Figure 3.5**, along with the associated standard

error. The two modalities show the same general trend with degeneration grade: as degeneration grade

increases, the measured area of the NP decreases. Nonparametric statistical tests were performed

(Statistica 10.0): the Mann-Whitney (M-W) U test and Wilcoxon (W) test were used to compare

independent and dependent groups respectively, and the Spearman r test was used to assess

correlations between variables. NP areas were found to be significantly smaller in Grade 4 discs

compared to Grade 3 discs for both the ADC maps (pM-W<0.0001) and $T2_w$ (pM-W<0.0001) images,

while differences in NP areas were insignificant between Grade 2 and 3 for both ADC maps (pM-W=0.49)

and $T2_w$ (pM-W=0.05). However, the NP areas identified by $T2_w$ imaging and ADC maps within each

grade were determined to be significantly different, with ADC being consistently larger (pW<0.0001 for

all grades). To account for potential overestimation of ADC disc area due to lower resolution of ADC

maps compared to $T2_w$ images, an erosion procedure was applied to the ADC NP mask to remove any

potential smeared pixel regions around the perimeter of the mask. Even with this potential source of

error removed, area estimates between ADC and $T2_w$ images were still found to be significantly different

as determined via t-test (two-sample assuming equal variances, p< 0.05).

Figure 3.5 – Average measured NP area [mm^2] grouped by Pfirrmann grade as determined by T2w imaging (**black circle** + dotted line) and ADC maps (grey triangle + dashed line). Error bars represent standard error.

*Indicates significance determined by Wilcoxon (W) test (pW<0.0001).

**Indicates significance determined by Mann-Whitney (M-W) U test (pM-W<0.0001).
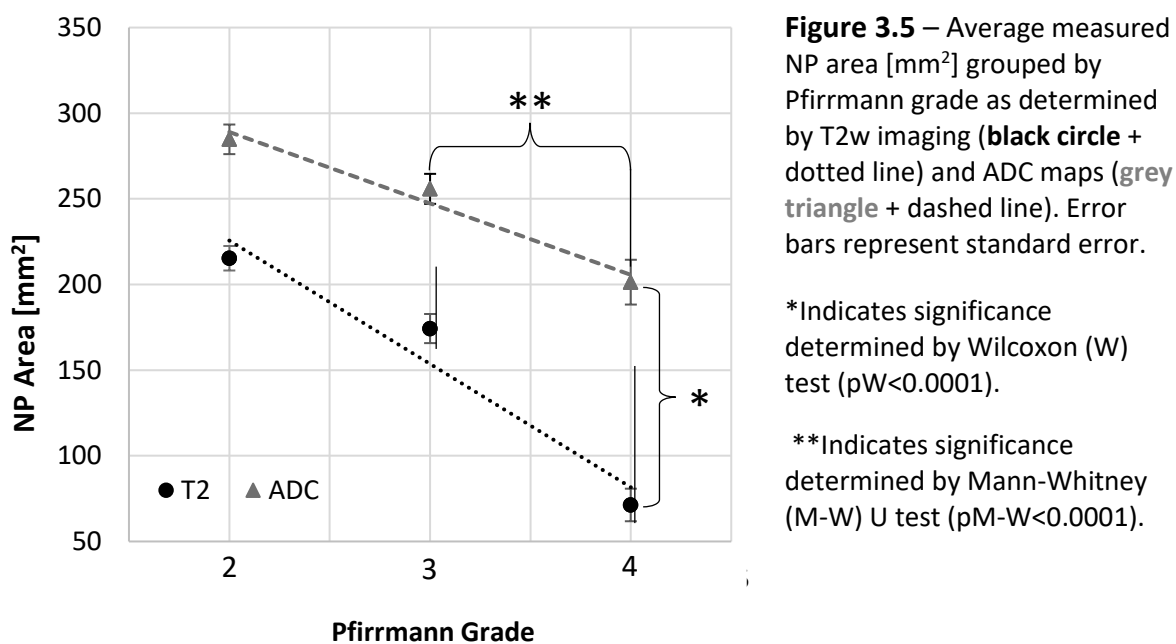
This behavior is also showcased in **Figure 3.6**, where $T2_w$ imaging results for NP area are plotted against

the ADC map results. This figure showcases both the general trends and the data contribution from each

disc.
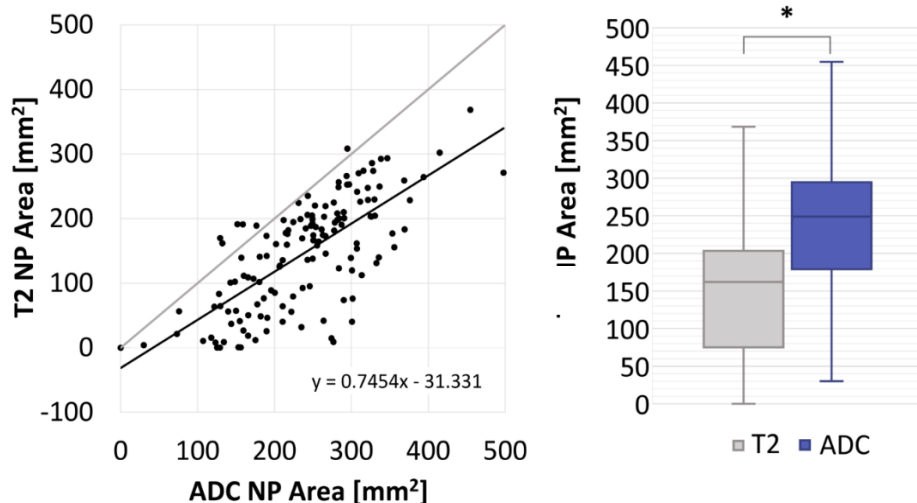
Figure 3.6 – NP area [mm^2] as measured by T2w imaging and ADC maps. *Left:* average area [mm^2] of the NP calculated from processing T2$_w$ images vs. ADC maps (n = 141 discs), equation shown on plot. Light grey line indicates the result if the NP areas calculated from T2$_w$ images and ADC Map are equal. *Right:* Bar graph of NP area calculated from T2$_w$ imaging and ADC maps. Error bars represent SEM. Significance (*) determined via t-test (two-sample assuming equal variances).

The average intensity of the nucleus was also collected for both ADC maps and T2$_w$ images (**Figure 3.7**).

Some patients were excluded due to lack of adequately visible spinal fluid area for normalization. The NP

intensity range for T2$_w$ images was 0.1 to 0.7, and <0.1 to 0.8 for ADC maps.
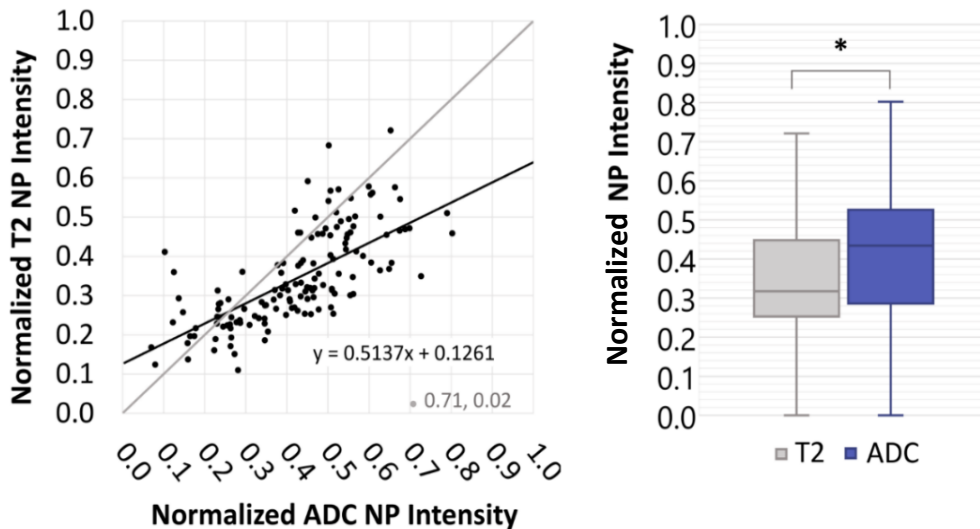
Figure 3.7 – Normalized NP intensity as measured by T2w imaging and ADC maps. *Left: a*verage normalized NP intensity determined from ROIs of equal area taken of each disc (n = 134 discs) in T1$_w$ images vs. ADC maps. Associated equation shown on plot. NP intensity was normalized to the spinal fluid. *Right:* Bar graph of average normalized NP intensity calculated from T2$_w$ imaging and ADC maps. Error bars represent SEM. Significance (*) determined via t-test (two-sample assuming equal variances).

Discussion

In this investigation, analysis of pixel variation was used to test the hypothesis that: (1) the distribution of MRI signal intensity within the IVD depends on the spinal pathology (and its severity), and (2) ADC is more sensitive than $T2_w$ images for this purpose. The first portion of the hypothesis was found to be unanimously true for both imaging modalities, as shown in **Figure 3.5**. This result agrees with the literature and indicates a baseline sensitivity of both modalities at recognizing degeneration in the NP. However, ADC maps consistently identified a significantly larger NP area within each grade of degeneration for all 3 levels of all 47 patients. This demonstrates that the two modalities have fundamentally different capabilities for NP visualization and indicates that one must be more accurate than the other. Furthermore, the differences between the measured areas increased with progressing degeneration, with a maximum difference of 180 mm^2 in Grade 4. This indicates that one modality is more sensitive to degenerated tissue. Furthermore, the intensity measurements also indicate a difference between the two modalities. The range of intensities captured was smaller for $T2_w$ images compared to ADC maps, indicating that ADC maps had a greater contrast range. This is also supported by the trendline of the data which has a slope of less than 1, indicating that the majority of the points fell below the grey line (which indicates a 1:1 equivalence). In practical terms, this result means that the NP was frequently visualized as brighter in the ADC maps compared to the $T2_w$ images, making it easier to distinguish. Though, using the same logic, it appears that at some very low intensities the NP is more visible in the $T2_w$ images than on ADCs. However, this is likely a misleading result: these low-intensity data points represent the most severely degenerated discs, which would have likely lost most of their NP tissue. In this case, the AF could be mistakenly measured on the $T2_w$ image, whereas in the ADC map, the AF isn't visualized and so only the background noise is recorded, resulting in a lower value for NP intensity relative to the $T2_w$ image.

These results indicate that ADC maps may be better at visualizing the NP tissue during advanced degeneration when it is dehydrated or partially sequestered/herniated because it cannot be obscured by the AF. The hypothesis that ADC is a sensitive measure of NP tissue is supported by preliminary findings

in other work being done by our research group which showed that ADC values had significant correlation with steady state nutrient concentrations in the disc as determined by a 2D computational model of transport in the disc using real patient data. However, this hypothesis cannot be fully evaluated until the relative accuracy of each of these modalities is directly and quantitatively assessed. This is a limitation of the current work which future animal models will attempt to address.

Another potential limitation of the present work is the prominent noise present in the DWI imaging, which, though mitigated through application of a median filter, could have skewed results. This possibility should be further investigated with histogram analysis of empty areas of the image (i.e., background) to quantify the variability due to noise. If the variability introduced due to noise causes the error bars to overlap, this could indicate substantial skewing of the results. Should this prove to be an issue, future experiments should be conducted with a stronger MRI unit (2 Tesla or more) to minimize the amount of noise. Additionally, though the manual IVD segmentation technique used in this work is sufficient for these purposes, use of more automated methods in the future could improve consistency of segmentation and save time.

Conclusions

This work describes a method for quantitative comparison of T2$_w$ imaging and ADC maps as tools for evaluating intervertebral disc degeneration. Specifically, the average pixel intensity and mid-sagittal cross-sectional area of the nucleus were extracted and quantified for direct comparison between the modalities. The results demonstrated a significant difference between the two modalities in terms of NP area identified within each Pfirrmann Grade of degeneration. Furthermore, this difference increased with progressive stages of degeneration. This indicates that one modality is definitively superior at visualizing the nucleus through its degenerative changes. We hypothesize this to be ADC maps, which may allow for more precise and accurate identification of the NP compared to T2-weighted images due to their heightened sensitivity to tissue hydration. This requires further validation, which will be the focus of a

planned future animal model study in which bovine tail motion segments will be used to directly compare imaging results to tissue samples.

Future Work

Validation of the imaging results is required to determine the true relative accuracy of the two modalities at identifying NP tissue. The proposed methodology will specifically make use of ex-vivo bovine tail motion segments to compare imaging data directly to physiological tissue measurements. Tails will be cleaned and prepared for imaging by first removing all extraneous tissue (muscles, tendons, ligaments, etc.) from the motion segment. Following cleaning, the spines will be set in agar, ensuring they are aligned to enable easy capture of mid-sagittal slices (**Figure 3.8**). The images of the animal model will be processed with the same protocol specified for the patient images. Shortly after imaging (to minimize differences in results due to dehydration and degeneration of the excised tissue), the bovine tails will be processed for histology according to the staining method described by Grunert et al.(2015),[140] which should aid in visual distinction between AF and NP tissues. The area of the NP will be recorded for each disc, along with the disc level and associated degeneration grade. The measured areas will be normalized to the cross sectional area of the entire disc to correct for any tissue dehydration or warping which occurs during the embedding and staining process. This area can then be directly compared to the areas measured from both modalities to determine which modality is in better agreement with the physiological reality, and therefore which is the superior modality for evaluation of IVD degeneration.
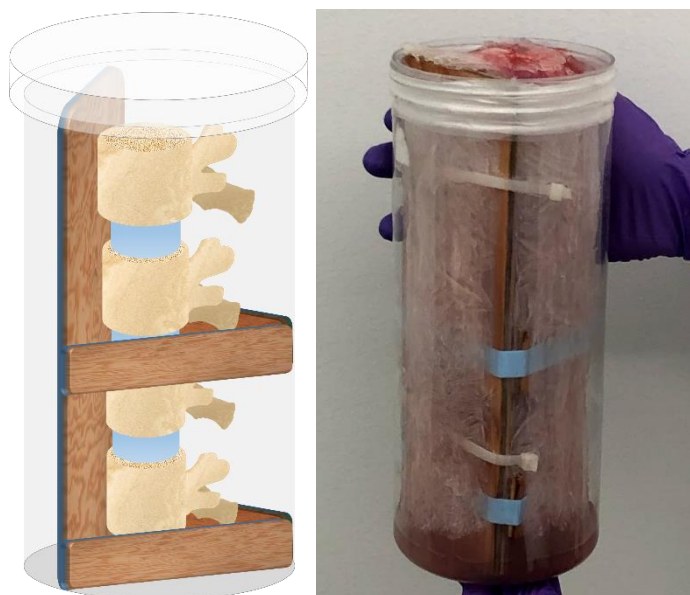
Figure 3.8 – Bovine tail imaging preparation.

Chapter 4: General Conclusions

Two major research questions were investigated in this work: (1) does directly incorporating patient data into solute transport models generate sufficiently unique results to indicate improved IVD characterization and model accuracy, and (2) are ADC maps comparable or better for visualization of the nucleus pulposus compared to the clinical gold standard of $T2_w$ imaging. To address the first question, patient-specific NP diffusivities were extracted using ADC maps and incorporated into a 3D transport model developed in COMSOL Multiphysics (version 5.3a). This enabled the calculation of patient-specific steady state distribution of nutrients and metabolites withing the disc. Distinct differences in solute distribution were apparent between patients, even within discs of the same Pfirrmann grade. This indicates that the patient-specific diffusivities in each disc greatly influenced the resulting metabolite gradients in the disc, beyond what can be captured using generic data from literature. An updated version of the model, which has more dynamic geometry capabilities, is already showing even more dramatic differences as a function of patient-specific disc morphology. These results indicate the value of patient-specific treatments and supports the incorporation of more personalized medicine techniques for LBP treatment. Next steps for this work include validation of the model results using human IVDs; this validation is essential prior to using this model to influence therapeutic techniques in a clinical setting. This will be accomplished using a custom IVD bioreactor which is capable of axially loading the discs to mimic the *in vivo* loading patterns observed in humans. The validation process could also be used to test the relative acuracy of different versions of the model, for example: comparing a version which includes a cell death model in addition to transport and metabolism models. This will allow the model to be optimized for efficiency and accuracy.

Considering the high variability in efficacy surrounding current treatment methods for LBP, it is incumbent on research and medical communities alike to further investigate the efficacy and best practices for existing treatments and push to develop new therapies centered around treating the root cause of LBP, rather than just relieving its symptoms. Biological therapies are the new horizon for treatment of LBP

caused by disc degeneration, and the technologies investigated here could prove crucial in developing and refining best practices for administration of those therapies. Pending this further development, this model could be a great asset to researchers and clinicians alike as a tool to predict the nutrient environment in the disc as a result of specific degenerative changes or novel biological treatments.

The model showcased in Chapter 2 relies on DWI images and resulting ADC maps to incorporate patient specific diffusivities. This brought us to our second research question: how accurate is ADC mapping at visualizing the NP? To address this question, quantitative analysis of pixel variation was performed in Chapter 3 to investigate potential differences between ADC mapping and the current clinical gold standard of $T2_w$. Specifically, each modality was used to quantitatively measure the NP pixel intensity and mid-sagittal cross-sectional area. Manual segmentation techniques and histogram-based thresholding were used to separate the NP from surrounding structures including the AF and endplates. Once the NP was isolated, the mid-sagittal cross-sectional area and average pixel intensity were measured. The results for each disc were directly compared between modalities, and additionally plotted against Pfirrmann grade to check for correlations with degeneration. The results of the degeneration study agree with the trends shown in previous literature, namely that as degeneration grade increases, the measured area of the NP decreases. This indicates a general sensitivity of both modalities to degeneration of the NP; however, ADC maps consistently identified a significantly larger NP area within each degeneration grade. This demonstrates that the two modalities have fundamentally different capabilities for NP visualization and implies that one is more accurate than the other.

Because ADC is sensitive to changes in the water and proteoglycan content, we hypothesize this might allow for more precise and accurate visualization of the NP compared to $T2_w$ images, and therefore make it the superior modality. This determination will be the focus of upcoming validation work which will use animal models to directly compare imaging results to tissue dimensions and morphology. To the best of author's knowledge, the fundamental accuracy of both these modalities has yet to be properly validated against tissue samples, so this validation experiment will not only answer the current research question,

but also provide valuable knowledge on the relative accuracy of $T2_w$ imaging for NP visualization, which is the most common modality used in a clinical setting and the current gold standard for disc herniation visualization. Pending results of these next steps, ADC maps could then be used to evaluate patient discs more accurately for degeneration prior to treatment, enabling more accurate diagnosis, and therefore, more targeted and effective treatments. This is especially the case for novel biological therapies, where efficacy may be strongly dependent on an accurate assessment of disc-specific nutrient limitations.

The overall focus of the work presented here was to investigate key characteristics of the human IVD and the technologies and techniques which can be used to capture, evaluate, and model those characteristics. This work establishes a foundation for future studies into patient-specific models and therapies and lays the groundwork for further validation of IVD visualization techniques. The overarching goal of this work of better understanding transport within the disc microenvironment to inform research practices and clinical patient evaluation and treatment for disc degeneration and LBP. The better the patient data collection techniques, the better the model predictions, and with a growing emphasis on precision medicine, this area of research will likely provide valuable tools for development of future therapies for disc degeneration.

Bibliography

1. Freburger JK, Holmes GM, Agans RP, et al. The Rising Prevalence of Chronic Low Back Pain. *Archives of Internal Medicine*. 2009;169(3):251-258. doi:10.1001/archinternmed.2008.543

2. Hoy D, March L, Brooks P, et al. The global burden of low back pain: estimates from the Global Burden of Disease 2010 study. *Ann Rheum Dis*. 2014;73(6):968-974. doi:10.1136/annrheumdis-2013-204428

3. Hoy D, Brooks P, Blyth F, Buchbinder R. The Epidemiology of low back pain. *Best Practice & Research Clinical Rheumatology*. 2010;24(6):769-781. doi:10.1016/j.berh.2010.10.002

4. Krismer M, van Tulder M. Low back pain (non-specific). *Best Practice & Research Clinical Rheumatology*. 2007;21(1):77-91. doi:10.1016/j.berh.2006.08.004

5. Huang Y-C, Urban JPG, Luk KDK. Intervertebral disc regeneration: do nutrients lead the way? *Nature Reviews Rheumatology*. 2014;10(9):561+.

6. Alkhatib B, Rosenzweig DH, Krock E, et al. Acute mechanical injury of the human intervertebral disc: link to degeneration and pain. *European cells & materials*. 2014;28:98-110.

7. Hughes SPF, Freemont AJ, Hukins DWL, McGregor AH, Roberts S. The pathogenesis of degeneration of the intervertebral disc and emerging therapies in the management of back pain. *The Journal of Bone and Joint Surgery British volume*. 2012;94-B(10):1298-1304. doi:10.1302/0301-620X.94B10.28986

8. Urban JP, Roberts S. Degeneration of the intervertebral disc. *Arthritis Res Ther*. 2003;5(3):120-130. doi:10.1186/ar629

9. Balagué F, Mannion AF, Pellisé F, Cedraschi C. Non-specific low back pain. *The Lancet*. 2012;379(9814):482-491. doi:10.1016/S0140-6736(11)60610-7

10. Zheng C-J, Chen J. Disc degeneration implies low back pain. *Theor Biol Med Model*. 2015;12. doi:10.1186/s12976-015-0020-3

11. Qaseem A, Wilt TJ, McLean RM, Forciea MA. Noninvasive Treatments for Acute, Subacute, and Chronic Low Back Pain: A Clinical Practice Guideline From the American College of Physicians. *Ann Intern Med*. 2017;166(7):514-530. doi:10.7326/M16-2367

12. Low Back Pain Fact Sheet | National Institute of Neurological Disorders and Stroke. Accessed January 20, 2021. https://www.ninds.nih.gov/Disorders/Patient-Caregiver-Education/Fact-Sheets/Low-Back-Pain-Fact-Sheet#3102_7

13. Malfliet A, Ickmans K, Huysmans E, et al. Best Evidence Rehabilitation for Chronic Pain Part 3: Low Back Pain. *J Clin Med*. 2019;8(7). doi:10.3390/jcm8071063

14. Ferreira PH, Ferreira ML, Maher CG, Herbert RD, Refshauge K. Specific stabilisation exercise for spinal and pelvic pain: a systematic review. *Aust J Physiother*. 2006;52(2):79-88. doi:10.1016/s0004-9514(06)70043-5

15. Gordon R, Bloxham S. A Systematic Review of the Effects of Exercise and Physical Activity on Non-Specific Chronic Low Back Pain. *Healthcare (Basel)*. 2016;4(2). doi:10.3390/healthcare4020022

16. Šarabon N, Palma P, Vengust R, Strojnik V. UČINKOVITOST SENZORIČNO-MOTORIČNE STABILIZACIJSKE VADBE TRUPA PRI PACIENTIH S KRONIČNO BOLEČINO V LEDVENEM DELU HRBTENICE: PILOTSKA ŠTUDIJA. Published online 2011:13.

17. Low Back Pain: Clinical Practice Guidelines Linked to the International Classification of Functioning, Disability, and Health from the Orthopaedic Section of the American Physical Therapy Association: Journal of Orthopaedic & Sports Physical Therapy: Vol 42, No 4. Accessed February 26, 2021. https://www.jospt.org/doi/10.2519/jospt.2012.42.4.A1

18. Advice to rest in bed versus advice to stay active for acute low-back pain and sciatica - PubMed. Accessed February 26, 2021. https://pubmed.ncbi.nlm.nih.gov/20556780/

19. Effects of exercise therapy in patients with acute low back pain: a systematic review of systematic reviews - PubMed. Accessed February 26, 2021. https://pubmed.ncbi.nlm.nih.gov/32795336/

20. Rajaee SS, Kanim LEA, Bae HW. National trends in revision spinal fusion in the USA: patient characteristics and complications. *Bone Joint J*. 2014;96-B(6):807-816. doi:10.1302/0301-620X.96B6.31149

21. Erdem MN, Erken HY, Aydogan M. The effectiveness of non-surgical treatments, re-discectomy and minimally invasive transforaminal lumbar interbody fusion in post-discectomy pain syndrome. *J Spine Surg*. 2018;4(2):414-422. doi:10.21037/jss.2018.04.02

22. Hedlund R, Johansson C, Hägg O, Fritzell P, Tullberg T, Swedish Lumbar Spine Study Group. The long-term outcome of lumbar fusion in the Swedish lumbar spine study. *Spine J*. 2016;16(5):579-587. doi:10.1016/j.spinee.2015.08.065

23. Guyer RD, Thongtrangan I, Ohnmeiss DD. Outcomes of CHARITE Lumbar Artificial Disk versus Fusion: 5-Year Data. *Seminars in Spine Surgery*. 2012;24(1):32-36. doi:10.1053/j.semss.2011.11.007

24. McAnany SJ, Overley SC, Anwar MA, et al. Comparing the Incidence of Index Level Fusion Following Minimally Invasive Versus Open Lumbar Microdiscectomy. *Global Spine J*. 2018;8(1):11-16. doi:10.1177/2192568217718818

25. Javid MJ, Hadar EJ. Long-term follow-up review of patients who underwent laminectomy for lumbar stenosis: a prospective study. *J Neurosurg*. 1998;89(1):1-7. doi:10.3171/jns.1998.89.1.0001

26. Overdevest G, Vleggeert-Lankamp C, Jacobs W, Thomé C, Gunzburg R, Peul W. Effectiveness of posterior decompression techniques compared with conventional laminectomy for lumbar stenosis. *Eur Spine J*. 2015;24(10):2244-2263. doi:10.1007/s00586-015-4098-4

27. Findlay GF, Hall BI, Musa BS, Oliveira MD, Fear SC. A 10-year follow-up of the outcome of lumbar microdiscectomy. *Spine (Phila Pa 1976)*. 1998;23(10):1168-1171. doi:10.1097/00007632-199805150-00019

28. Hiratzka J, Rastegar F, Contag AG, Norvell DC, Anderson PA, Hart RA. Adverse Event Recording and Reporting in Clinical Trials Comparing Lumbar Disk Replacement with Lumbar Fusion: A Systematic Review. *Global Spine J*. 2015;5(6):486-495. doi:10.1055/s-0035-1567835

29. Wong C-B, Chen W-J, Chen L-H, Niu C-C, Lai P-L. Clinical outcomes of revision lumbar spinal surgery: 124 patients with a minimum of two years of follow-up. *Chang Gung Med J*. 2002;25(3):175-182.

30. Castillo H, Chintapalli RTV, Boyajian HH, et al. Lumbar discectomy is associated with higher rates of lumbar fusion. *Spine J*. 2019;19(3):487-492. doi:10.1016/j.spinee.2018.05.016

31. Kerezoudis P, Goncalves S, Cesare JD, et al. Comparing outcomes of fusion versus repeat discectomy for recurrent lumbar disc herniation: A systematic review and meta-analysis. *Clin Neurol Neurosurg*. 2018;171:70-78. doi:10.1016/j.clineuro.2018.05.023

32. Bydon M, Macki M, Abt NB, et al. Clinical and surgical outcomes after lumbar laminectomy: An analysis of 500 patients. *Surg Neurol Int*. 2015;6(Suppl 4):S190-193. doi:10.4103/2152-7806.156578

33. Siepe CJ, Heider F, Wiechert K, Hitzl W, Ishak B, Mayer MH. Mid- to long-term results of total lumbar disc replacement: a prospective analysis with 5- to 10-year follow-up. *Spine J*. 2014;14(8):1417-1431. doi:10.1016/j.spinee.2013.08.028

34. Patel MS, Braybrooke J, Newey M, Sell P. A comparative study of the outcomes of primary and revision lumbar discectomy surgery. *Bone Joint J*. 2013;95-B(1):90-94. doi:10.1302/0301-620X.95B1.30413

35. Owens RK, Djurasovic M, Onyekwelu I, Bratcher KR, McGraw KE, Carreon LY. Outcomes and revision rates in normal, overweight, and obese patients 5 years after lumbar fusion. *Spine J*. 2016;16(10):1178-1183. doi:10.1016/j.spinee.2016.06.005

36. Delitto A, George SZ, Van Dillen L, et al. Low Back Pain. *J Orthop Sports Phys Ther*. 2012;42(4):A1-A57. doi:10.2519/jospt.2012.42.4.A1

37. low-back-pain-reference-guide.pdf. Accessed February 26, 2021. https://ichom.org/files/medical-conditions/low-back-pain/low-back-pain-reference-guide.pdf

38. Resnik L, Dobrzykowski E. Guide to outcomes measurement for patients with low back pain syndromes. *J Orthop Sports Phys Ther*. 2003;33(6):307-316; discussion 317-318. doi:10.2519/jospt.2003.33.6.307

39. Stamm TA, Boesendorfer A, Omara M, Ritschl V, Štefanac S, Mosor E. Outcomes research in non-specific low back pain. *Wien Klin Wochenschr*. 2019;131(21):550-557. doi:10.1007/s00508-019-1523-4

40. Common Terminology Criteria for Adverse Events (CTCAE) | Protocol Development | CTEP. Accessed February 26, 2021. https://ctep.cancer.gov/protocoldevelopment/electronic_applications/ctc.htm

41. Rampersaud YR, Neary MA, White K. Spine adverse events severity system: content validation and interobserver reliability assessment. *Spine (Phila Pa 1976)*. 2010;35(7):790-795. doi:10.1097/BRS.0b013e3181bf25a3

42. Arnau JM, Vallano A, Lopez A, Pellisé F, Delgado MJ, Prat N. A critical review of guidelines for low back pain treatment. *Eur Spine J*. 2006;15(5):543-553. doi:10.1007/s00586-005-1027-y

43. Kim LH, Vail D, Azad TD, et al. Expenditures and Health Care Utilization Among Adults With Newly Diagnosed Low Back and Lower Extremity Pain. *JAMA Netw Open*. 2019;2(5):e193676. doi:10.1001/jamanetworkopen.2019.3676

44. Puhl AA, Reinhart CJ, Rok ER, Injeyan HS. An Examination of the Observed Placebo Effect Associated with the Treatment of Low Back Pain – A Systematic Review. Pain Research and Management. doi:https://doi.org/10.1155/2011/625315

45. Turner JA, Deyo RA, Loeser JD, Von Korff M, Fordyce WE. The importance of placebo effects in pain treatment and research. *JAMA*. 1994;271(20):1609-1614.

46. Pincus T, Vlaeyen JWS, Kendall NAS, Von Korff MR, Kalauokalani DA, Reis S. Cognitive-Behavioral Therapy and Psychosocial Factors in Low Back Pain: Directions for the Future. *Spine*. 2002;27(5):E133.

47. Clays E, De Bacquer D, Leynen F, Kornitzer M, Kittel F, De Backer G. The Impact of Psychosocial Factors on Low Back Pain: Longitudinal Results From the Belstress Study. *Spine*. 2007;32(2):262-268. doi:10.1097/01.brs.0000251884.94821.c0

48. Chan C, Peng P. Failed Back Surgery Syndrome. *Pain Medicine*. 2011;12(4):577-606. doi:10.1111/j.1526-4637.2011.01089.x

49. Failed back surgery syndrome: current perspectives. - PubMed - NCBI. Accessed March 19, 2019. https://www.ncbi.nlm.nih.gov/pubmed/27853391

50. Verbeek J, Sengers M-J, Riemens L, Haafkens J. Patient Expectations of Treatment for Back Pain: A Systematic Review of Qualitative and Quantitative Studies. *Spine*. 2004;29(20):2309-2318. doi:10.1097/01.brs.0000142007.38256.7f

51. Oegema TR. Biochemistry of the intervertebral disc. *Clin Sports Med*. 1993;12(3):419-439.

52. Shapiro IM, Risbud MV. *The Intervertebral Disc: Molecular and Structural Studies of the Disc in Health and Disease*. Springer; 2013. https://books.google.com/books?id=SFEbswEACAAJ

53. Giers MB, Munter BT, Eyster KJ, et al. Biomechanical and Endplate Effects on Nutrient Transport in the Intervertebral Disc. *World Neurosurg*. 2017;99:395-402. doi:10.1016/j.wneu.2016.12.041

54. Magnier C, Boiron O, Wendling-Mansuy S, Chabrand P, Deplano V. Nutrient distribution and metabolism in the intervertebral disc in the unloaded state: A parametric study. *Journal of Biomechanics*. 2009;42(2):100-108. doi:10.1016/j.jbiomech.2008.10.034

55. Kolluru GK, Bir SC, Kevil CG. Endothelial Dysfunction and Diabetes: Effects on Angiogenesis, Vascular Remodeling, and Wound Healing. *Int J Vasc Med*. 2012;2012. doi:10.1155/2012/918267

56. Cardiovascular Diseases - How Tobacco Smoke Causes Disease: The Biology and Behavioral Basis for Smoking-Attributable Disease - NCBI Bookshelf. Accessed March 18, 2019. https://www.ncbi.nlm.nih.gov/books/NBK53012/

57. Urban J PG, Smith S CT, Fairbank J CT. Nutrition of the Intervertebral Disc. *Spine*. 2004;29(23):2700-2709.

58. Urban JPG, Grunhagen T, Wilde G, Soukane DM, Shirazi-Adl SA, Urban JPG. Nutrient supply and intervertebral disc metabolism. *Journal of Bone and Joint Surgery*. 2006;88(Supplement 2):30. doi:10.2106/JBJS.E.01290

59. Bibby S RS, Jones D A, Ripley R M, Urban J PG. Metabolism of the Intervertebral Disc: Effects of Low Levels of Oxygen, Glucose, and pH on Rates of Energy Metabolism of Bovine Nucleus Pulposus Cells. *Spine*. 2005;30(5):487-496.

60. Mokhbi Soukane D, Shirazi-Adl A, Urban JPG. Computation of coupled diffusion of oxygen, glucose and lactic acid in an intervertebral disc. *Journal of Biomechanics*. 2007;40(12):2645-2654.

61. Ferguson SJ, Ito K, Nolte L-P. Fluid flow and convective transport of solutes within the intervertebral disc. *Journal of Biomechanics*. 2004;37(2):213-221. doi:10.1016/S0021-9290(03)00250-1

62. Malandrino A, Noailly J, Lacroix D. The Effect of Sustained Compression on Oxygen Metabolic Transport in the Intervertebral Disc Decreases with Degenerative Changes (Sustained Compression on Oxygen Transport in IVD). *PLoS Computational Biology*. 2011;7(8):e1002112. doi:10.1371/journal.pcbi.1002112

63. Jackson AR, Yuan T-Y, Huang C-Y, Gu WY. A Conductivity Approach to Measuring Fixed Charge Density in Intervertebral Disc Tissue. *Ann Biomed Eng*. 2009;37(12):2566-2573. doi:10.1007/s10439-009-9792-0

64. Zhu Q, Jackson AR, Gu WY. Cell viability in intervertebral disc under various nutritional and dynamic loading conditions: 3d Finite element analysis. *Journal of Biomechanics*. 2012;45(16):2769-2777. doi:https://doi.org/10.1016/j.jbiomech.2012.08.044

65. Gullbrand E, Peterson T, Ahlborn P, et al. ISSLS Prize Winner: Dynamic Loading–Induced Convective Transport Enhances Intervertebral Disc Nutrition. *Spine*. 2015;40(15):1158-1164. doi:10.1097/BRS.0000000000001012

66. Munter B. Demonstration of the Effects of Traction Therapy on the Nutrient Supply of the Lumbar Intervertebral Disc: A Mathematical Model. Published online 2016.

67. Lootus M, Kadir T, Zisserman A. Radiological Grading of Spinal MRI. :12.

68. Maus T. Imaging the back pain patient. *Phys Med Rehabil Clin N Am*. 2010;21(4):725-766. doi:10.1016/j.pmr.2010.07.004

69. Roudsari B, Jarvik JG. Lumbar Spine MRI for Low Back Pain: Indications and Yield. *American Journal of Roentgenology*. 2010;195(3):550-559. doi:10.2214/AJR.10.4367

70. Chou R, Fu R, Carrino JA, Deyo RA. Imaging strategies for low-back pain: systematic review and meta-analysis. *The Lancet*. 2009;373(9662):463-472. doi:10.1016/S0140-6736(09)60172-0

71. Ash LM, Modic MT, Obuchowski NA, Ross JS, Brant-Zawadzki MN, Grooff PN. Effects of Diagnostic Information, Per Se, on Patient Outcomes in Acute Radiculopathy and Low Back Pain. *American Journal of Neuroradiology*. 2008;29(6):1098-1103. doi:10.3174/ajnr.A0999

72. Balasubramanya R, Selvarajan SK. Lumbar Spine Imaging. In: *StatPearls*. StatPearls Publishing; 2020. Accessed January 13, 2021. http://www.ncbi.nlm.nih.gov/books/NBK553181/

73. de Schepper EIT, Damen J, van Meurs JBJ, et al. The Association Between Lumbar Disc Degeneration and Low Back Pain: The Influence of Age, Gender, and Individual Radiographic Features. *Spine*. 2010;35(5):531-536. doi:10.1097/BRS.0b013e3181aa5b33

74. McKinnis LN. *Fundamentals of Musculoskeletal Imaging*. F.A. Davis; 2013.

75. Heidari P, Farahbakhsh F, Rostami M, Noormohammadpour P, Kordi R. The Role of Ultrasound in Diagnosis of the Causes of Low Back Pain: a Review of the Literature. *Asian J Sports Med*. 2015;6(1). doi:10.5812/asjsm.23803

76. Johannessen W, Auerbach JD, Wheaton AJ, et al. Assessment of Human Disc Degeneration and Proteoglycan Content Using T1ρ-weighted Magnetic Resonance Imaging. *Spine (Phila Pa 1976)*. 2006;31(11):1253-1257. doi:10.1097/01.brs.0000217708.54880.51

77. Paul CPL, Smit TH, Graaf M de, et al. Quantitative MRI in early intervertebral disc degeneration: T1rho correlates better than T2 and ADC with biomechanics, histology and matrix content. *PLOS ONE*. 2018;13(1):e0191442. doi:10.1371/journal.pone.0191442

78. Zuo J, Joseph GB, Li X, et al. In-vivo Intervertebral Disc Characterization using Magnetic Resonance Spectroscopy and T1ρ Imaging: Association with Discography and Oswestry Disability Index and SF-36. *Spine (Phila Pa 1976)*. 2012;37(3):214-221. doi:10.1097/BRS.0b013e3182294a63

79. Kolf A-K, Konieczny M, Hesper T, et al. T2* Mapping of the Adult Intervertebral Lumbar Disc: Normative Data and Analysis of Diurnal Effects. *J Orthop Res*. 2019;37(9):1956-1962. doi:10.1002/jor.24327

80. Huang L, Liu Y, Ding Y, et al. Quantitative evaluation of lumbar intervertebral disc degeneration by axial T2∗ mapping. *Medicine (Baltimore)*. 2017;96(51). doi:10.1097/MD.0000000000009393

81. Trattnig S, Stelzeneder D, Goed S, et al. Lumbar intervertebral disc abnormalities: comparison of quantitative T2 mapping with conventional MR at 3.0 T. *Eur Radiol*. 2010;20(11):2715-2722. doi:10.1007/s00330-010-1843-2

82. Blumenkrantz G, Zuo J, Li X, Kornak J, Link TM, Majumdar S. In vivo 3.0-tesla magnetic resonance T1ρ and T2 relaxation mapping in subjects with intervertebral disc degeneration and clinical symptoms. *Magnetic Resonance in Medicine*. 2010;63(5):1193-1200. doi:https://doi.org/10.1002/mrm.22362

83. Mengiardi B, Schmid MR, Boos N, et al. Fat Content of Lumbar Paraspinal Muscles in Patients with Chronic Low Back Pain and in Asymptomatic Volunteers: Quantification with MR Spectroscopy. *Radiology*. 2006;240(3):786-792. doi:10.1148/radiol.2403050820

84. Byvaltsev VA, Stepanov IA, Kalinin AA, Shashkov KV. Diffusion-Weighted Magnetic Resonance Tomography in the Diagnosis of Intervertebral Disk Degeneration. *Biomed Eng*. 2016;50(4):253-256. doi:10.1007/s10527-016-9632-0

85. Chen P, Wu C, Huang M, et al. Apparent Diffusion Coefficient of Diffusion-Weighted Imaging in Evaluation of Cervical Intervertebral Disc Degeneration: An Observational Study with 3.0 T Magnetic Resonance Imaging. BioMed Research International. doi:https://doi.org/10.1155/2018/6843053

86. Kettler A, Wilke H-J. Review of existing grading systems for cervical or lumbar disc and facet joint degeneration. *Eur Spine J*. 2006;15(6):705-718. doi:10.1007/s00586-005-0954-y

87. Thompson JP, Pearce RH, Schechter MT, Adams ME, Tsang IK, Bishop PB. Preliminary evaluation of a scheme for grading the gross morphology of the human intervertebral disc. *Spine (Phila Pa 1976)*. 1990;15(5):411-415. doi:10.1097/00007632-199005000-00012

88. Boos N, Weissbach S, Rohrbach H, Weiler C, Spratt KF, Nerlich AG. Classification of age-related changes in lumbar intervertebral discs: 2002 Volvo Award in basic science. *Spine (Phila Pa 1976)*. 2002;27(23):2631-2644. doi:10.1097/00007632-200212010-00002

89. Lane NE, Nevitt MC, Genant HK, Hochberg MC. Reliability of new indices of radiographic osteoarthritis of the hand and hip and lumbar disc degeneration. *J Rheumatol*. 1993;20(11):1911-1918.

90. Pfirrmann CW, Metzdorf A, Zanetti M, Hodler J, Boos N. Magnetic resonance classification of lumbar intervertebral disc degeneration. *Spine*. 2001;26(17):1873-1878.

91. Gunzburg R, Parkinson R, Moore R, et al. A cadaveric study comparing discography, magnetic resonance imaging, histology, and mechanical behavior of the human lumbar disc. *Spine (Phila Pa 1976)*. 1992;17(4):417-426. doi:10.1097/00007632-199204000-00007

92. Disc Height and Segmental Motion as Risk Factors for Recurre... : Spine. Accessed January 30, 2021. https://journals.lww.com/spinejournal/Abstract/2009/11150/Disc_Height_and_Segmental_Motion_as_Risk_Factors.13.aspx

93. Ordway NR, Seymour R, Donelson RG, Hojnowski L, Lee E, Edwards TW. Cervical Sagittal Range-of-Motion Analysis Using Three Methods: Cervical Range-of-Motion Device, 3Space, and Radiography. *Spine*. 1997;22(5):501-508.

94. Been E, Kalichman L. Lumbar lordosis. *The Spine Journal*. 2014;14(1):87-97. doi:10.1016/j.spinee.2013.07.464

95. Luoma K, Vehmas T, Riihimäki H, Raininko R. Disc Height and Signal Intensity of the Nucleus Pulposus on Magnetic Resonance Imaging as Indicators of Lumbar Disc Degeneration. *Spine*. 2001;26(6):680-686.

96. McAuliffe MJ, Lalonde FM, McGarry D, Gandler W, Csaky K, Trus BL. Medical Image Processing, Analysis and Visualization in clinical research. In: *Proceedings 14th IEEE Symposium on Computer-Based Medical Systems. CBMS 2001*. ; 2001:381-386. doi:10.1109/CBMS.2001.941749

97. Fortin M, Dobrescu O, Jarzem P, Ouellet J, Weber MH. Quantitative Magnetic Resonance Imaging Analysis of the Cervical Spine Extensor Muscles: Intrarater and Interrater Reliability of a Novice and an Experienced Rater. *Asian Spine J*. 2018;12(1):94-102. doi:10.4184/asj.2018.12.1.94

98. Kyrölä KK, Salme J, Tuija J, Tero I, Eero K, Arja H. Intra- and Interrater Reliability of Sagittal Spinopelvic Parameters on Full-Spine Radiographs in Adults With Symptomatic Spinal Disorders. *Neurospine*. 2018;15(2):175-181. doi:10.14245/ns.1836054.027

99. Wallwork TL, Hides JA, Stanton WR. Intrarater and Interrater Reliability of Assessment of Lumbar Multifidus Muscle Thickness Using Rehabilitative Ultrasound Imaging. *Journal of*

Orthopaedic & Sports Physical Therapy. Published online October 1, 2007. doi:10.2519/jospt.2007.2418

100. Alomari RS, Corso JJ, Chaudhary V. Labeling of Lumbar Discs Using Both Pixel- and Object-Level Features With a Two-Level Probabilistic Model. *IEEE Transactions on Medical Imaging*. 2011;30(1):1-10. doi:10.1109/TMI.2010.2047403

101. Yushkevich PA, Piven J, Hazlett HC, et al. User-guided 3D active contour segmentation of anatomical structures: Significantly improved efficiency and reliability. *NeuroImage*. 2006;31(3):1116-1128. doi:10.1016/j.neuroimage.2006.01.015

102. Giulietti G, Summers PE, Ferraro D, Porro CA, Maraviglia B, Giove F. Semiautomated segmentation of the human spine based on echoplanar images. *Magnetic Resonance Imaging*. 2011;29(10):1429-1436. doi:10.1016/j.mri.2011.08.006

103. Erdil E, Yagci AM, Argunsah AÖ, et al. A tool for automatic dendritic spine detection and analysis. Part I: Dendritic spine detection using multi-level region-based segmentation. In: *2012 3rd International Conference on Image Processing Theory, Tools and Applications (IPTA)*. ; 2012:167-171. doi:10.1109/IPTA.2012.6469558

104. Chevrefils C, Chériet F, Grimard G, Aubin C-E. Watershed Segmentation of Intervertebral Disk and Spinal Canal from MRI Images. In: Kamel M, Campilho A, eds. *Image Analysis and Recognition*. Lecture Notes in Computer Science. Springer; 2007:1017-1027. doi:10.1007/978-3-540-74260-9_90

105. Mateusiak M, Mikolajczyk K. Semi-automatic Spine Segmentation Method of CT Data. In: Szewczyk R, Krejsa J, Nowicki M, Ostaszewska-Liżewska A, eds. *Mechatronics 2019: Recent Advances Towards Industry 4.0*. Advances in Intelligent Systems and Computing. Springer International Publishing; 2020:29-35. doi:10.1007/978-3-030-29993-4_4

106. Tsai M-D, Jou S-B, Hsieh M-S. A new method for lumbar herniated inter-vertebral disc diagnosis based on image analysis of transverse sections. *Computerized Medical Imaging and Graphics*. 2002;26(6):369-380. doi:10.1016/S0895-6111(02)00033-2

107. Korez R, Likar B, Pernuš F, Vrtovec T. Model-Based Segmentation of Vertebral Bodies from MR Images with 3D CNNs. In: Ourselin S, Joskowicz L, Sabuncu MR, Unal G, Wells W, eds. *Medical Image Computing and Computer-Assisted Intervention – MICCAI 2016*. Lecture Notes in Computer Science. Springer International Publishing; 2016:433-441. doi:10.1007/978-3-319-46723-8_50

108. Haq R, Aras R, Besachio DA, Borgie RC, Audette MA. 3D lumbar spine intervertebral disc segmentation and compression simulation from MRI using shape-aware models. *Int J CARS*. 2015;10(1):45-54. doi:10.1007/s11548-014-1094-9

109. Ragan D, Starkschall G, McNutt T, Kaus M, Guerrero T, Stevens CW. Semiautomated four-dimensional computed tomography segmentation using deformable models. *Medical Physics*. 2005;32(7Part1):2254-2261. doi:https://doi.org/10.1118/1.1929207

110. Hesamian MH, Jia W, He X, Kennedy P. Deep Learning Techniques for Medical Image Segmentation: Achievements and Challenges. *J Digit Imaging*. 2019;32(4):582-596. doi:10.1007/s10278-019-00227-x

111. Patil P, Dong Q, Wang D, et al. Systemic clearance of p16INK4a-positive senescent cells mitigates age-associated intervertebral disc degeneration. *Aging Cell*. 2019;18(3):e12927. doi:https://doi.org/10.1111/acel.12927

112. van Deursen JM. The role of senescent cells in ageing. *Nature*. 2014;509(7501):439-446. doi:10.1038/nature13193

113. Vaudreuil N, Henrikson K, Pohl P, et al. Photopolymerizable biogel scaffold seeded with mesenchymal stem cells: safety and efficacy evaluation of novel treatment for intervertebral disc degeneration. *Journal of Orthopaedic Research*. 2019;37(6):1451-1459. doi:https://doi.org/10.1002/jor.24208

114. Sheyn D, Ben-David S, Tawackoli W, et al. Human iPSCs can be differentiated into notochordal cells that reduce intervertebral disc degeneration in a porcine model. *Theranostics*. 2019;9(25):7506-7524. doi:10.7150/thno.34898

115. Hodgkinson T, Shen B, Diwan A, Hoyland JA, Richardson SM. Therapeutic potential of growth differentiation factors in the treatment of degenerative disc diseases. *JOR SPINE*. 2019;2(1):e1045. doi:https://doi.org/10.1002/jsp2.1045

116. Ouyang Z-H, Wang W-J, Yan Y-G, Wang B, Lv G-H. The PI3K/Akt pathway: a critical player in intervertebral disc degeneration. *Oncotarget*. 2017;8(34):57870-57881. doi:10.18632/oncotarget.18628

117. Lin C-Y, Crowley ST, Uchida S, Komaki Y, Kataoka K, Itaka K. Treatment of Intervertebral Disk Disease by the Administration of mRNA Encoding a Cartilage-Anabolic Transcription Factor. *Molecular Therapy - Nucleic Acids*. 2019;16:162-171. doi:10.1016/j.omtn.2019.02.012

118. Banala RR, Vemuri SK, Dar GH, et al. Efficiency of dual siRNA-mediated gene therapy for intervertebral disc degeneration (IVDD). *The Spine Journal*. 2019;19(5):896-904. doi:10.1016/j.spinee.2018.10.016

119. Wang J, Nisar M, Huang C, et al. Small molecule natural compound agonist of SIRT3 as a therapeutic target for the treatment of intervertebral disc degeneration. *Experimental & Molecular Medicine*. 2018;50(11):1-14. doi:10.1038/s12276-018-0173-3

120. Cheng X, Zhang L, Zhang K, et al. Circular RNA VMA21 protects against intervertebral disc degeneration through targeting miR-200c and X linked inhibitor-of-apoptosis protein. *Annals of the Rheumatic Diseases*. 2018;77(5):770-779. doi:10.1136/annrheumdis-2017-212056

121. Hebelka H, Lagerstrand K, Brisby H, et al. The importance of level stratification for quantitative MR studies of lumbar intervertebral discs: a cross-sectional analysis in 101 healthy adults. *Eur Spine J*. 2019;28(9):2153-2161. doi:10.1007/s00586-019-06059-1

122. Sharma A, Walk RE, Tang SY, Eldaya R, Owen PJ, Belavy DL. Variability of T2-Relaxation Times of Healthy Lumbar Intervertebral Discs is More Homogeneous within an Individual Than across Healthy Individuals. *American Journal of Neuroradiology*. 2020;41(11):2160-2165. doi:10.3174/ajnr.A6791

123. Belykh E, Kalinin AA, Patel AA, et al. Apparent diffusion coefficient maps in the assessment of surgical patients with lumbar spine degeneration. *PLOS ONE*. 2017;12(8):e0183697. doi:10.1371/journal.pone.0183697

124. Chilla GS, Tan CH, Xu C, Poh CL. Diffusion weighted magnetic resonance imaging and its recent trend—a survey. *Quant Imaging Med Surg*. 2015;5(3):407-422. doi:10.3978/j.issn.2223-4292.2015.03.01

125. Le Bihan D, Breton E. In vivo magnetic resonance imaging of diffusion. *Comptes Rendus des Seances de l'Academie des Sciences Serie 2*. 1985;301(15):1109-1112.

126. Soukane DM, Shirazi-Adl A, Urban JP. Analysis of Nonlinear Coupled Diffusion of Oxygen and Lactic Acid in Intervertebral Discs. *Journal of Biomechanical Engineering*. 2005;127(7):1121-1126. doi:10.1115/1.2073674

127. Fundamentals of Momentum, Heat, and Mass Transfer, Revised 6th Edition. Wiley.com. Accessed March 19, 2019. https://www.wiley.com/en-us/Fundamentals+of+Momentum%2C+Heat%2C+and+Mass+Transfer%2C+Revised+6th+Edition-p-9781118947463

128. Harris KR, Woolf LA. Pressure and temperature dependence of the self diffusion coefficient of water and oxygen-18 water. *J Chem Soc, Faraday Trans 1*. 1980;76(0):377-385. doi:10.1039/F19807600377

129. Das DB, Welling A, Urban JPG, Boubriak OA. Solute Transport in Intervertebral Disc. *Annals of the New York Academy of Sciences*. 2009;11611(1):44-61.

130. Gilbert HTJ, Hodson N, Baird P, Richardson SM, Hoyland JA. Acidic pH promotes intervertebral disc degeneration: Acid-sensing ion channel -3 as a potential therapeutic target. *Sci Rep*. 2016;6. doi:10.1038/srep37360

131. Sakai D, Schol J. Cell therapy for intervertebral disc repair: Clinical perspective. *Journal of Orthopaedic Translation*. 2017;9:8-18. doi:10.1016/j.jot.2017.02.002

132. Section 2, Chapter 6: Current Biologic Therapies for the Treatment of Lumbar Intervertebral Disc Disease. Wheeless' Textbook of Orthopaedics. Published April 20, 2018. Accessed December 9, 2020. https://www.wheelessonline.com/issls/section-2-chapter-6-current-biologic-therapies-for-the-treatment-of-lumbar-intervertebral-disc-disease/

133. Jackson AR, Huang C-YC, Brown MD, Yong Gu W. 3D Finite Element Analysis of Nutrient Distributions and Cell Viability in the Intervertebral Disc: Effects of Deformation and Degeneration. *Journal of Biomechanical Engineering*. 2011;133(091006). doi:10.1115/1.4004944

134. Shalash W, Ahrens SR, Bardonova LA, Byvaltsev VA, Giers MB. Patient Specific Models of Nutrient Availability in Degenerated Intervertebral Discs. *In revision*. Published online 2021.

135. Humphreys SC, Eck JC. Clinical Evaluation and Treatment Options for Herniated Lumbar Disc. *AFP*. 1999;59(3):575.

136. Diffusion weighted imaging | Radiology Reference Article | Radiopaedia.org. Accessed December 8, 2019. https://radiopaedia.org/articles/diffusion-weighted-imaging-1?lang=us

137. Chen C, Huang M, Han Z, et al. Quantitative T2 Magnetic Resonance Imaging Compared to Morphological Grading of the Early Cervical Intervertebral Disc Degeneration: An Evaluation Approach in Asymptomatic Young Adults. *PLoS One*. 2014;9(2). doi:10.1371/journal.pone.0087856

138. Waldenberg C, Hebelka H, Brisby H, Lagerstrand KM. MRI histogram analysis enables objective and continuous classification of intervertebral disc degeneration. *Eur Spine J*. 2018;27(5):1042-1048. doi:10.1007/s00586-017-5264-7

139. Stelzeneder D, Welsch GH, Kovács BK, et al. Quantitative T2 evaluation at 3.0T compared to morphological grading of the lumbar intervertebral disc: A standardized evaluation approach in patients with low back pain. *European Journal of Radiology*. 2012;81(2):324-330. doi:10.1016/j.ejrad.2010.12.093

140. Grunert P, Hudson KD, Macielak MR, et al. Assessment of Intervertebral Disc Degeneration Based on Quantitative MRI Analysis: an in vivo study. *Spine (Phila Pa 1976)*. 2014;39(6):E369-E378. doi:10.1097/BRS.0000000000000194

141. Niu G, Yang J, Wang R, Dang S, Wu EX, Guo Y. MR Imaging Assessment of Lumbar Intervertebral Disk Degeneration and Age-Related Changes: Apparent Diffusion Coefficient versus T2 Quantitation. *American Journal of Neuroradiology*. 2011;32(9):1617-1623. doi:10.3174/ajnr.A2556

142. Bloem JL, Reijnierse M, Huizinga TWJ, Mil AHM van der H. MR signal intensity: staying on the bright side in MR image interpretation. *RMD Open*. 2018;4(1):e000728. doi:10.1136/rmdopen-2018-000728

143. Aissiou M, Périé D, Mac-Thiong J-M. Normalized intervertebral disc MRI signal as a biomarker of pain. *Journal of Biomedical Science and Engineering*. 2013;06(03):372-380. doi:10.4236/jbise.2013.63A047

144. Julien G, Delphine P, Stefan P, Hubert L, Carl-Eric A. MRI signal distribution within the intervertebral disc as a biomarker of adolescent idiopathic scoliosis and spondylolisthesis. *BMC Musculoskeletal Disorders*. 2012;13(1):239. doi:10.1186/1471-2474-13-239

145. Luoma K, Vehmas T, Grönblad M, Kerttula L, Kääpä E. MRI follow-up of subchondral signal abnormalities in a selected group of chronic low back pain patients. *Eur Spine J*. 2008;17(10):1300-1308. doi:10.1007/s00586-008-0716-8

146. Drake-Pérez M, Delattre BMA, Boto J, et al. Normal Values of Magnetic Relaxation Parameters of Spine Components with the Synthetic MRI Sequence. *American Journal of Neuroradiology*. 2018;39(4):788-795. doi:10.3174/ajnr.A5566

Appendices

Appendix 1 – Index of Abbreviations

Table A1.1 – List of abbreviations used in this work.

ABBREVIATION	TERM	ABBREVIATION	TERM
ADC	Apparent diffusion coefficient	NSLBP	Non-specific Low Back Pain
AF	Annulus Fibrosis	OA	Outer annulus
BEP	Bony endplate	ODI	Oswestry Disability Index
CEP	Cartilaginous endplate	RMQ/RMD	Roland-Morris Disability Questionnaire
COPM	Canadian Occupational Performance Measure	ROI	Region of Interest
CTCAE	Common Terminology Criteria for Adverse Events	SAVES	Spine Adverse Events Severity System
DWI	Diffusion weighted imaging	SEM	Standard error of the mean
ECM	Extracellular matrix	TENS	Transcutaneous Electrical Nerve Stimulation
EP	Endplate	T2$_w$	T2-weighted imaging
GA	Global Assessment	VAS	Visual Analogue Scale
HRQL	Health-Related Quality of Life		
IA	Inner annulus		
ICC	Interclass Correlation Coefficients		
IVD	Intervertebral disc		
LBP	Lower back pain		
MRI	Magnetic resonance imaging		
NP	Nucleus pulposus		

Appendix 2 – Supplemental Figures

Figure A2.2 – From Huang et al (2014): Pathways of nutrient supply in a normal intervertebral disc.
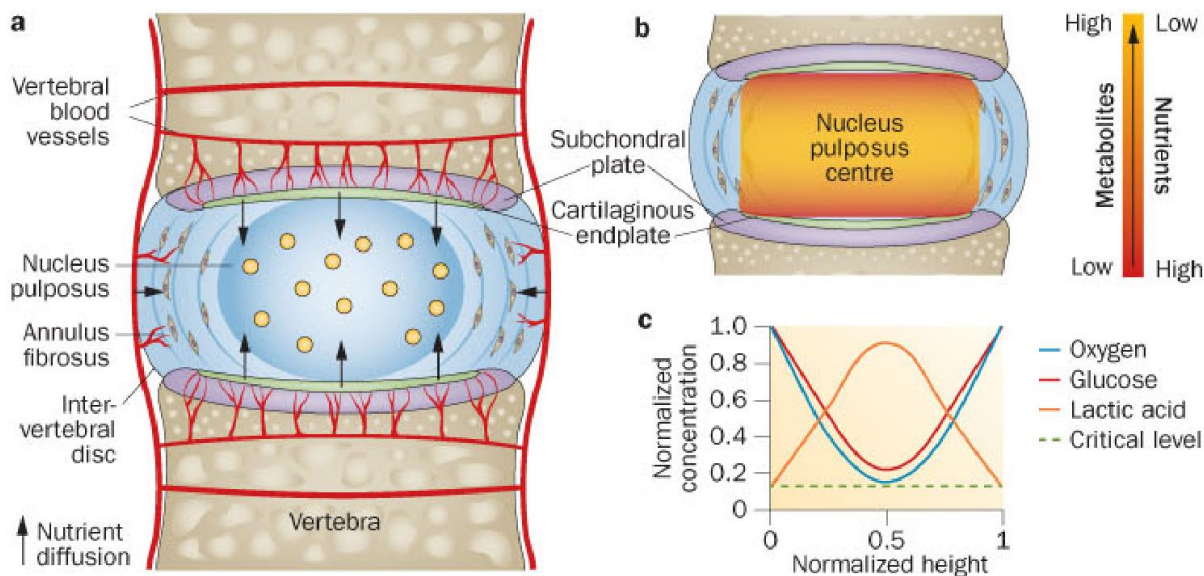
a. From Huang et al (2014): "Cells of the avascular disc nucleus pulposus and inner annulus fibrosis are supplied by vertebral blood vessels. Capillaries penetrate the subchondral plate through marrow spaces and terminate in loops at the junction of the subchondral plate and cartilaginous endplate. Nutrients (e.g. oxygen and glucose) diffuse from the capillary bed through the cartilaginous endplate under gradients arising from metabolic demands of disc cells, while metabolic wastes (e.g. lactic acid) diffuse in the reverse direction. Cells of the outer annulus fibrosis are supplies by capillaries from blood vessels in the surrounding soft tissues that penetrate a few millimeters into the disc."[5]

b. From Huang et al (2014): "The center of the disc has the lowest levels of nutrients and highest concentration of metabolites."[5]

c. From Huang et al (2014): "Schematic showing normalized concentration gradients of glucose, oxygen, and lactic acid across the nucleus, endplate to endplate. Nutrient concentrations must remain above the critical levels to maintain cell viability and activity."[5]

Figure A2.2 – From Urrutia et al: algorithm used for grading lumbar disc degeneration[147]

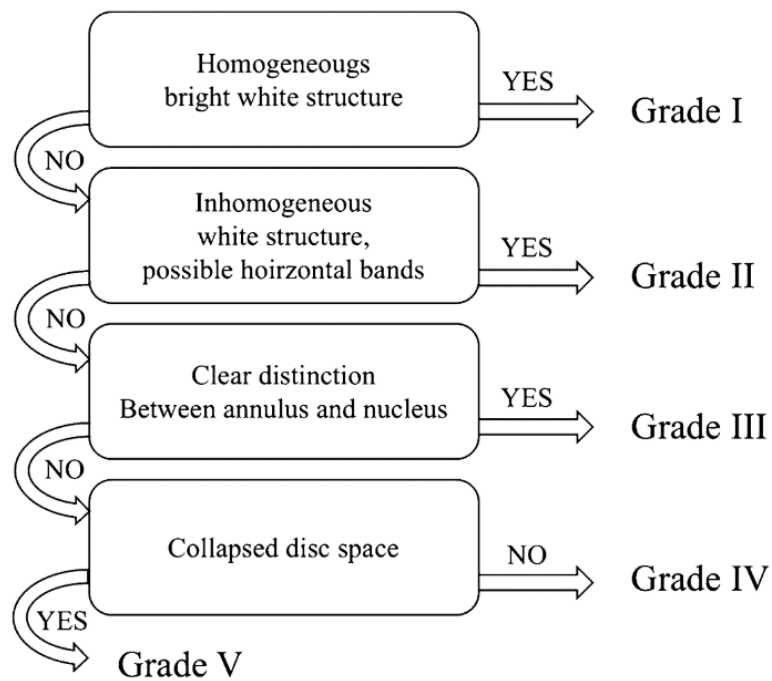**Figure A2.3** – Sectioned and labeled porcine lumbar IVD. Disc isolation and sagittal slicing was performed by undergraduate research assistance Rees Rosene. Color coded section geometry provided for reference: cancellous bone (purple), cortical bone (red), the CEP (blue), OA and IA (orange and yellow), and the NP (green). The axis of symmetry (r=0) for the 2D axisymmetric model is shown in red.
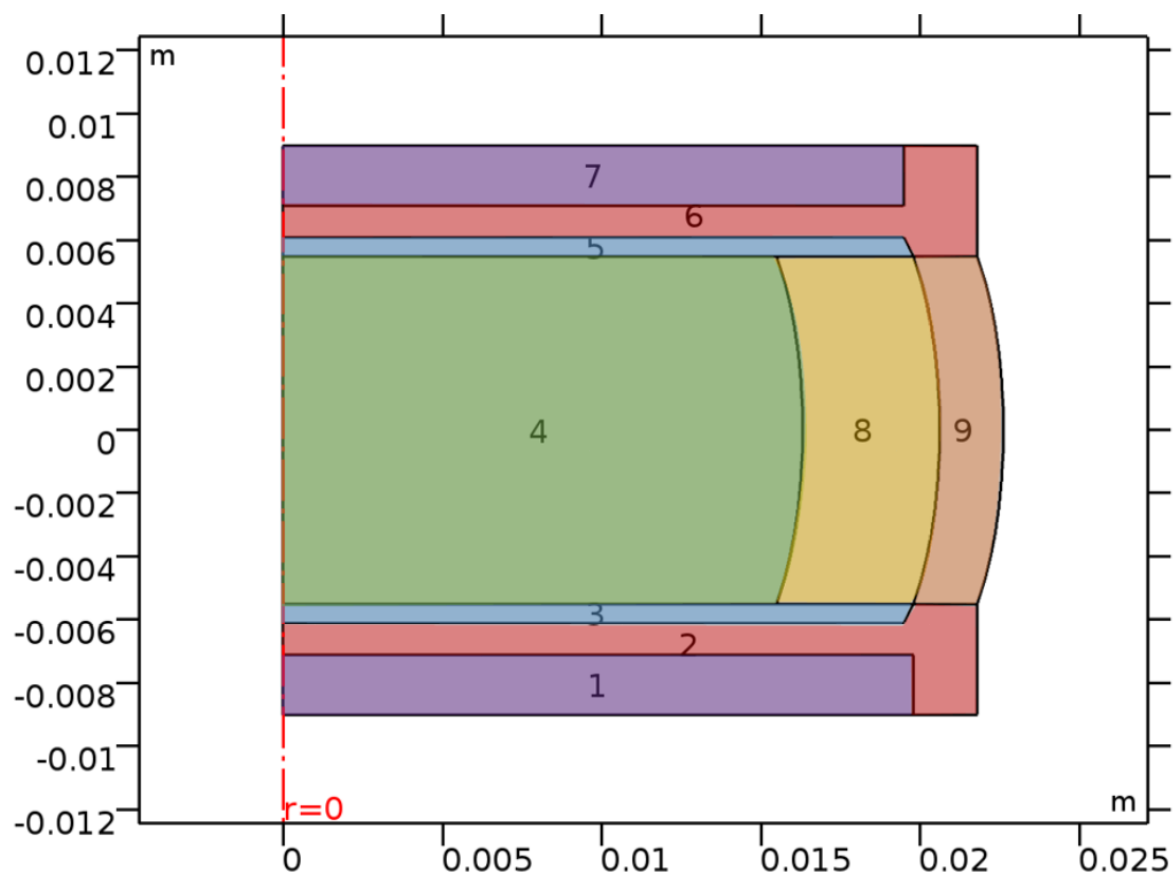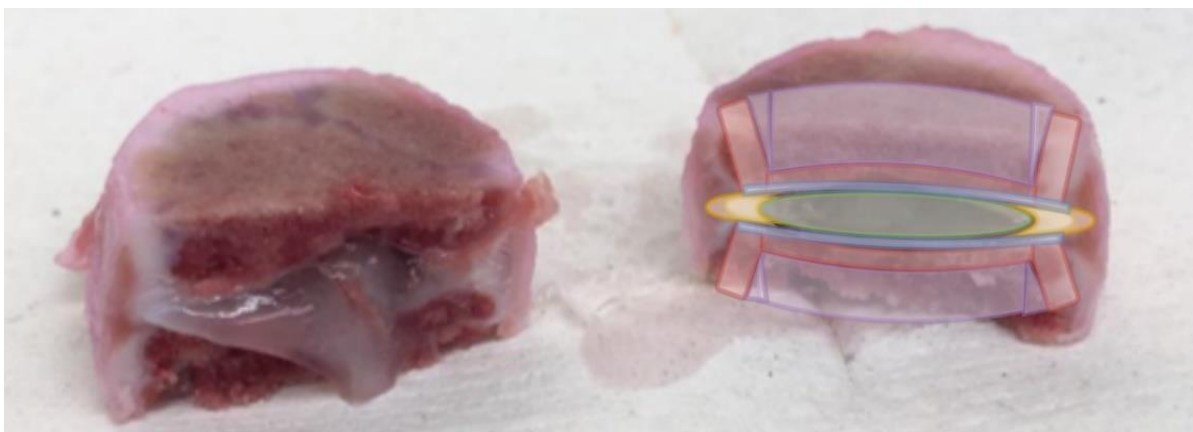
Appendix 3 – Supplemental Tables

Table A3.1 – Rubric for adverse events. Final scores were a combination of adverse event severity and frequency.

No significant adverse effect	*Assuming that the treatment is not conducted incorrectly or inappropriately.
Mild adverse event	**Results in symptoms which are mildly uncomfortable/irritating:** ex. rhinitis, small increases in pain, muscle soreness, headache, heartburn.
Moderate adverse event	**Results in symptoms which substantially impact daily life and may require medical intervention, but do not require hospitalization:** ex. nausea, fever, diarrhea, sedation, dizziness.
Severe adverse event	**Results in symptoms which require immediate/prolonged medical intervention, surgery and/or hospitalization:** ex. addiction, tissue necrosis, ulcer, bleeding, reherniation.
Serious adverse event	**Results in permanent disability and/or life threatening event, or death:** ex. life-threatening hemorrhage, limb amputation, death.

Table A3.2 – Summary of variables used in model, including their value, unit, and a short description.

COMSOL Variables	Value	Unit	Description
ADCmap	an1(r,z)		References the ADC image in cylindrical geometry
C_CEP	1.56E-05		Ratio of cell density (CEP/NP) * conversion from nmol to mol * conversion from mm^3 to m^3 * conversion from h to s[126]
C_IAF	2.50E-06		Ratio of cell density (AF/NP) * conversion from nmol to mol * conversion from mm^3 to m^3 * conversion from h to s[126]
C_NP	1.11E-06		Ratio of cell density (NP/NP) * conversion from nmol to mol * conversion from mm^3 to m^3 * conversion from h to s[126]
C_OAF	1.00E-05		Ratio of cell density (AF/NP) * conversion from nmol to mol * conversion from mm^3 to m^3 * conversion from h to s[126]
CD_CEP	1.50E-02	million cells/mm^3	Cell Density[126]
CD_IA	0.006	million cells/mm^3	Cell Density[126]
CD_NP	0.004	million cells/mm^3	Cell Density[126]
CD_OA	0.012	million cells/mm^3	Cell Density[126]
Dg_AF	2.85E-10	m²/s	Diffusion constant for glucose[126]
Dg_CEP	2.11E-10	m²/s	Diffusion constant for glucose[126]
Dg_CNB	2.11E-09	m²/s	Diffusion constant for glucose[126]
Dg_CTB	2.11E-11	m²/s	Diffusion constant for glucose[126]
Dg_NP	ADCmap		References image (Literature value =1.81E-09)[126]
DGW	0.98		Conversion factor for ADC data to glucose
Dl_AF	4.24E-10	m²/s	Diffusion constant for lactate[126]
Dl_CEP	3.14E-10	m²/s	Diffusion constant for lactate[126]
Dl_CNB	3.14E-09	m²/s	Diffusion constant for lactate[126]
Dl_CTB	3.14E-11	m²/s	Diffusion constant for lactate[126]
Dl_NP	ADCmap		References image (Literature value =5.61E-10[126])
DLW	0.46		Conversion factor for ADC data to lactate
Do_AF	1.15E-09	m²/s	Diffusion constant for oxygen[126]
Do_CEP	5.08E-10	m²/s	Diffusion constant for oxygen[126]
Do_CNB	5.08E-09	m²/s	Diffusion constant for oxygen[126]
Do_CTB	5.08E-11	m²/s	Diffusion constant for oxygen[126]
Do_NP	ADCmap		References image (Literature value =1.65E-09[126])
DOW	0.98		Conversion factor for ADC data to oxygen
E_CEP	0.6		Water Content[126]
E_IA	0.73		Water Content[126]

Table A3.2 (Continued) – Summary of variables used in model, including their value, unit, and a short description.

COMSOL Variables	Value	Unit	Description
E_NP	**0.8**		**Water Content[126]**
E_OA	0.66		Water Content[126]
G	c_g	mol/m³	Concentration of glucose
L	c_l	mol/m³	Concentration of lactate
log	10		Exponent value for glucose reaction term
ltog	-0.0005		Conversion factor from L to G reaction
O	c_o	mol/m³	Concentration of oxygen
O2_MAX	0.053	mol/m³	Maximum O2 concentration in blood (6.4 kPa converted to a concentration using Henry's Law) [126]
R_G	tdsg.R_c_g	mol/(m³·s)	References reaction term for glucose

Tables A3.3-A3.5 – Reaction terms for lactic acid, oxygen and glucose as they are entered into the COMSOL model.

Table A3.3 – Reaction terms for lactic acid used in the COMSOL model.

Region of Interest	*Lactic Acid*
CEP	(-1.5)*(tdsg.R_c_g)
NP	(-1.5)*(tdsg.R_c_g)
IA	(-1.5)*(tdsg.R_c_g)
OA	(-1.5)*(tdsg.R_c_g)

Table A3.4 – Reaction terms for oxygen used in the COMSOL model.

Region of Interest	*Oxygen*
CEP	-C_CEP*E_CEP*((7.28*(O/O2_MAX)*((8.05-0.1*(-L)) - 4.95))/ (1.46+(O/O2_MAX) + 4.03*((7.4-0.1*(-L))-4.95)))
NP	-C_NP*E_NP*((7.28*(O/O2_MAX)*((8.05-0.1*(L)) - 4.95))/(1.46+(O/O2_MAX)+ 4.03*((8.05-0.1*(L))-4.95)))
IA	-C_IAF*E_IA*((7.28*(O/O2_MAX)*((7.4-0.1*(L)) - 4.95))/ (1.46+(O/O2_MAX)+ 4.03*((7.4-0.1*(L))-4.95)))
OA	-C_OAF*E_OA*((7.28*(O/O2_MAX)*((7.4-0.1*(L)) -4.95))/ (1.46+(O/O2_MAX)+ 4.03*((7.4-0.1*(L))-4.95)))

Table A3.5 – Reaction terms for glucose used in the COMSOL model.

Region of Interest	Glucose
CEP	ltog*C_CEP*log^((-2.47)+((0.93)*(8.05-0.1*L))+((0.16)*(O/O2_MAX))-((0.0058)*((O/O2_MAX)^2)))
NP	ltog*C_NP*log^((-2.47)+((0.93)*(8.05-0.1*L))+((0.16)*(O/O2_MAX))-((0.0058)*((O/O2_MAX)^2)))
IA	ltog*C_IAF*log^((-2.47)+((0.93)*(8.05-0.1*L))+((0.16)*(O/O2_MAX))-((0.0058)*((O/O2_MAX)^2)))
OA	ltog*C_OAF*log^((-2.47)+((0.93)*(8.05-0.1*L))+((0.16)*(O/O2_MAX))-((0.0058)*((O/O2_MAX)^2)))

Table A3.6 – Metabolite concentration extrema changes with NP cell density. Cell densities for the rest of the IVD tissues were kept at the levels used in the original model: OA = 9.00E+06 (million cells/m^3), IA = 6.00E+06 (million cells/m^3) and CEP = 1.50E+07 (million cells/m^3).

NP Cell Density (million cells/m^3)	Glucose min [mol/m^3]	Lactate max [mol/m^3]	Oxygen min [mol/m^3]
4.00E+03	1.625	4.650	0.029
4.00E+05	1.541	4.743	0.028
1.20E+06	1.367	4.941	0.027
2.00E+06	1.178	5.145	0.026
2.80E+06	0.881	5.375	0.024
3.60E+06	0.525	5.744	0.022
4.00E+06	**0.350**	**5.958**	**0.022**
4.40E+06	0.177	6.174	0.021
5.20E+06	-0.157	6.600	0.019
6.00E+06	-0.475	7.012	0.018
6.80E+06	-0.778	7.407	0.017
7.60E+06	-1.067	7.786	0.016
8.00E+06	-1.207	7.969	0.015